The Dissertation Committee for Xiaohan Li certifies that this is the approved version of the following dissertation:

High Efficiency III/V Thin Film Solar Cells:

Light Trapping, Antireflection, and Band Structure Engineering

Committee:

Edward T. Yu, Supervisor

Seth R. Bank

S. V. Sreenivasan

Ananth Dodabalapur

Daniel Schaadt

High Efficiency III/V Thin Film Solar Cells:

Light Trapping, Antireflection, and Band Structure Engineering

by

Xiaohan Li, B.E.; M.S.E.

Dissertation

Presented to the Faculty of the Graduate School of

The University of Texas at Austin

in Partial Fulfillment

of the Requirements

for the Degree of

Doctor of Philosophy

The University of Texas at Austin

May, 2015

Dedication

To my family

Acknowledgements

I would like to thank my supervisor Dr. Edward T. Yu for his constant support throughout my Ph.D. journey. I would not have completed this dissertation without his broad knowledge, insightful suggestions, patient guidance, and warm encouragement. His rigorous scholarship and efficient work-style will benefit me in the future.

I would like to thank Dr. Seth R. Bank, Dr. S. V. Sreenivasan, Dr. Ananth Dodabalapur, and Dr. Daniel Schaadt for serving as my committee members and for their insightful comments on my dissertation work.

I would like to thank my collaborators Dr. Vaishno Dasika from Dr. Seth R. Bank's group, and Dr. Dongzhi Hu from Dr. Daniel Schaadt's group. Their dedicated work on III/V epi-growth made things happen. Also, I would like to thank Dr. Rao Tatavarti from Microlink Devices, Inc. and Dr. Kimberly Sablon from U. S. Army Research Laboratory for their constant guidance and support on our collaboration.

I would like to express my special thanks to Dr. Katsuaki Tanabe (The University of Tokyo) for his patient guidance and valuable suggestions on the III/V thin-film microelectronics fabrication process, which helped me overcome the most difficult time of my Ph.D. journey.

I would like to acknowledge the rest of current and former nanoscale characterization and devices group members: Ping-Chun Li, Li Ji, Clay McPheeters, Keunwoo Park, Lei Zhu, Chengqing Hu, Chris Brennan, Zhongjian Zhang, Gabe Cossio, and Heng-Lu Chang. I enjoyed lab days over the years with all of you.

I would like to thank staff members for the Microelectronics Research Center, including Dr. Marylene Palard, Dr. Ferrer Domingo, Mr. Johnny Johnson, Mr. Ricardo Garcia, and Mr. William Ostler for equipment training and maintenance.

I would also like to thank all my friends both inside and outside U. S., who have made my Ph.D. journey rich and colorful: Xingyu Zhang, Jingsi Li, Jaehyun Ahn, Yi Zou, Yusi Chen, Xin Zhao, Yifan Jiang, Kwangsub Byun, Boxue Chen, Yao-Feng Chang, Josh Guo, Shijie Zhou, Sheng Wen; and Yu Liu, Haolu Hu, Yan Chen, Wenjia Zhang, Hongyun Wang, Tingguang Chen, Yue Yin, Grace Yuan support from China.

Finally but not least, I would like to express my gratitude for my parents. It is them who always listen to my complaints and console me and help me get through various difficulties in my Ph.D. journey during these years.

High Efficiency III/V Thin-Film Solar Cells:

Light Trapping, Antireflection, and Band Structure Engineering

Xiaohan Li, Ph.D.

The University of Texas at Austin, 2015

Supervisor: Edward T. Yu

Photon management via submicron and subwavelength nanostructures has been extensively studied over the last decade, and has become one of the most important approaches of boosting the energy conversion efficiency for thin-film photovoltaic devices. The incorporation of low dimensional nanostructures, such as GaAs/InGaAs quantum wells, into typical GaAs single-junction cells will extend the cell absorption further into the sub-GaAs bandgap region but usually results in reduced cell open-circuit voltage. As a consequence, various bandgap engineering techniques for improving the energy conversion efficiency for quantum well solar cells have been reported. This dissertation will describe studies of light trapping in multiple GaAs/InGaAs quantum well solar cells via nanostructured front side dielectric coating and back side metal/dielectric contacts, photovoltaic performance enhancement for bulk and flexible thin-film GaAs solar cells through subwavelength nanostructured antireflection coating, and bandgap engineering techniques for GaAs/InGaAs multiple quantum well solar cells.

In the study of nanostructured dielectric antireflection coatings, a 5.8% increase in short-circuit current density is observed for the GaAs/$In_{0.3}Ga_{0.7}As$ multiple quantum well

cell coated with TiO_2 nanostructured coating compared to the cell coated with conventional Si_3N_4 single-layer antireflection coating even in the presence of high surface recombination. Numerical simulation shows that as high as 13% increase in short-circuit current density can be achieved without surface recombination. In the study of GaAs/$In_{0.3}Ga_{0.7}As$ multiple quantum well solar cells integrated with nanostructured back side metal/dielectric contacts, as high as 2.9% per quantum well external quantum efficiency is achieved, significantly surpassing the 1% per quantum well external quantum efficiency typically observed in quantum well solar cells. In both studies, two major mechanisms contributing to the increased longer wavelength quantum well absorption have been elucidated: Fabry-Perot resonances and scattering into guided optical modes.

In application of subwavelength-scale optical nanostructures on bulk and flexible epitaxial lift-off GaAs solar cells for broadband, omnidirectional improvement of photovoltaic performance, 1.1× increase in short-circuit current density is observed for the bulk GaAs cell fully integrated with optical nanostructures compared to the unpatterned cell (1.09× increase in short-circuit current density for flexible epitaxial lift-off GaAs cell) at normal incidence, while 1.67× increase in short-circuit current density is observed (1.52× increase in short-circuit current density is observed for flexible epitaxial lift-off GaAs cell) at 80^o angle of incidence.

In the study of bandgap engineering strategies for improving the photovoltaic performance for GaAs/InGaAs multiple quantum well solar cells, a quantum well solar cell with graded quantum well depths, which has an average 18% indium concentration in quantum wells, is shown to yield improvements in both open-circuit voltage and short-

circuit current density compared to a GaAs/$In_{0.18}Ga_{0.82}As$ quantum well solar cell with constant quantum well depths across the intrinsic region. The results of this study suggest that such an approach can also be implemented in quantum well solar cells with more complex quantum well structures, such as ternary or quaternary quantum wells, where the conduction and valence band offsets of each quantum well can be simultaneously engineered.

Table of Contents

List of Figures

Chapter 1: Introduction

III/V solar cells play an indispensable role in photovoltaic energy harvesting for space applications, and are promising candidates for concentrating and next-generation photovoltaics in terrestrial settings. [1-5] Furthermore, because of recent advances in epitaxial-lift off techniques, which substantially reduce the cost of producing III/V thin-film solar cells by enabling substrate reuse after separating thin-film device layers from their growth substrates, [6-8] there is a growing interest in mechanically flexible, light-weight, high-efficiency III/V solar cells for electricity generation strategies such as concentrated photovoltaic (CPV) systems [9] and high-efficiency mobile solar devices. [10]

The reduction in absorbing layer thickness achievable with epitaxial lift-off and similar techniques can, however, result in a reduction in optical absorption efficiency, particularly at longer wavelengths. Light trapping techniques in thin-film solar cells via light scattering by nanostructured rear contacts, [11, 12] subwavelength-scale nanoparticles, [13, 14] and surface texturing [15, 16] have been demonstrated to be promising and highly effective for improving a solar cell's optical absorption efficiency, and therefore the short-circuit current density, as well as the open-circuit voltage through photon recycling effects. [55, 56] For example, we have demonstrated that light trapping techniques can be powerful approaches for increasing the long-wavelength absorption in thin-film quantum well solar cells, [17, 18] where optical absorption in the quantum well region is relatively low and can be increased only to a limited degree by increasing the

number of quantum wells in the device due to limitations in growth techniques and challenges in extraction of photo-generated carriers.

Reduction in optical absorption efficiency can also occur due to Fresnel reflection, particularly at large incident angles, and reflection losses can act as a major obstacle for achieving high efficiency photovoltaic systems. [19-21] Conventional planar multilayer thin-film antireflection coatings are only able to provide excellent antireflection performance under limited ranges of incident angles and wavelengths, [22] and the choice of thin-film materials with different refractive indices is limited by the range of materials that exist in nature, although certain nanostructured composites can provide a wider range of refractive indices. [23] Alternative approaches involve employing subwavelength nanostructures fabricated on substrates of either high [24, 25] or low [26, 27] refractive indices, which are able to show improved antireflection performance over larger ranges of incident angles and wavelengths by providing a graded refractive index profile between the incident medium and the substrate material.

Compared to conventional GaAs *pn* junction solar cells, higher cell efficiency can also be potentially achieved by insertion of low-dimensional structures, such as quantum wells, into the intrinsic region of a GaAs *p-i-n* solar cell, which can increase the short-circuit current density (J_{sc}) by extending the optical absorption wavelength into the sub-GaAs bandgap region. [28-32] However, such approaches are usually accompanied by a substantial reduction in the cell's open-circuit voltage, potentially due to lattice mismatch and associated defect formation, [33, 34] and due to reduced carrier extraction efficiency since quantum wells can also function as recombination centers for photo-generated

carriers. [35-37] Strain balance techniques [38, 39] and band-edge energy profile engineering strategies [40] have been employed to address these issues.

In this dissertation, numerical simulation and experimental demonstration of front and back-side light trapping structures, subwavelength antireflection nanostructures, and bandgap engineering techniques for III/V thin-film solar cells are described. With these light trapping structures, quantum well absorption can be greatly enhanced by coupling incident light, particularly at long-wavelengths, into optical guided modes and Fabry-Perot resonance modes within the semiconductor absorbing region. Measurements show that within the long-wavelength range for which absorption occurs only in the quantum wells, as high as 3% external quantum efficiency per quantum well can be achieved with light trapping structures in quantum well solar cells, significantly exceeding the 1% external quantum efficiency per quantum well typically observed. Second, the design, fabrication and optimization of a low cost, large-area, flexible subwavelength antireflection structure for polymer-packaged bulk and flexible epitaxial lift-off GaAs solar cells are demonstrated. Such an integrated antireflection structure is able to provide excellent broadband, omnidirectional antireflection performance, which is demonstrated to be a promising candidate for applications in highly compact, portable and wearable photovoltaic energy harvesting. Finally, this dissertation includes our study on engineered graded GaAs/InGaAs quantum well solar cells. It is shown that the GaAs/InGaAs quantum well solar cell with graded quantum well depths is able to achieve a substantially improved open-circuit voltage compared to a conventional quantum well solar cell with the same average quantum well composition while maintaining sufficient quantum well absorption in the longer wavelength range.

Part of section 2.1 was published in *Journal of Applied Physics* 2014, X. H. Li, P. –C. Li, D. Z. Hu, D. M. Schaadt and E. T. Yu. Part of section 2.2 was published in *Journal of Applied Physics* 2013, X. H. Li, P.-C Li, D. Z. Hu, D. M. Schaadt and E. T. Yu. Part of section 3.1 was published in *Progress in Photovoltaics: Research and Applications*, X. H. Li, P. –C. Li, L. Ji, C. Stender, C. McPheeters, S. R. Tatavarti, K. Sablon and E. T. Yu. Part of section 3.2 has been submitted to *Progress in Photovoltaics: Research and Applications.* Part of chapter 4 was published in *Applied Physics Letters* 2014, X. H. Li, V. D. Dasika, P. –C. Li, L. Ji, S. R. Bank, and E. T. Yu.

Chapter 2: Light Trapping in Thin-Film Quantum Well Solar Cells via Subwavelength Dielectric/Metal Nanostructures

2.1 MOTIVATION

Thin-film solar cells have been widely deployed in various photovoltaic applications because of several favorable attributes, which can include high structural flexibility, lower weight, and reduced material use. However, due to the significantly thinner cell thickness, optical absorption efficiency for thin-film solar cells can be low. The exploitation of metal and dielectric nanostructures for inducing light trapping has become one of the most efficient measures of increasing the optical absorption efficiency for thin-film solar cells and compensating the reduced material usage for thin-film solar cells.

Light trapping in thin-film solar cells via engineered metal and dielectric nanostructures has emerged as a highly promising and effective approach of improving the cell optical absorption efficiency. For typical GaAs *pin* junction solar cells, the absorption of sunlight energy can be extended into the sub-GaAs bandgap region by insertion of low dimensional nanostructures (GaAs/InGaAs quantum wells (QWs) in this dissertation) into the intrinsic region of GaAs solar cells. Figure 2.1 shows the optical absorption ranges of GaAs and GaAs/$In_{0.3}Ga_{0.7}As$ QWs in standard solar irradiance spectra (AM0, AM1.5D, and AM1.5G). It is observed that GaAs cell typically absorbs photons with wavelengths shorter than ~900nm, whilst the GaAs/$In_{0.3}Ga_{0.7}As$ QW cell is able to collect photons with wavelengths longer than 900nm. However, as the optical absorption efficiency in the QW region is usually low and can be increased only to a

limited degree by increasing the number of QWs, measures need to be taken to further improve the QW optical absorption efficiency.

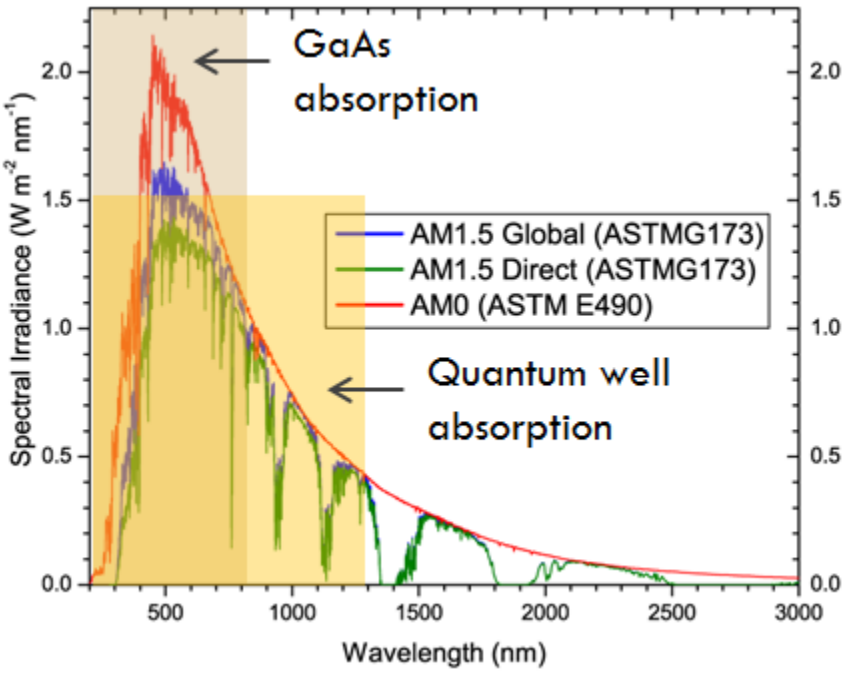

Figure 2.1. Standard solar irradiance spectra with GaAs and GaAs/$In_{0.3}Ga_{0.7}As$ quantum well absorption ranges schematically illustrated in grey and yellow boxes.

2.2 FRONT SIDE NANOSTRUCTURED ANTIREFLECTION COATINGS

In section 2.2, we discuss the numerical simulation, fabrication and measurement results for a TiO_2 nanostructured antireflection coating (ARC). Both simulation and measurement results show that the TiO_2 nanostructured ARC is able to provide an improved antireflection performance compared to a conventional single-layer silicon nitride thin-film ARC. Simulations reveal the physical mechanisms of the origin of photocurrent response enhancement at wavelengths longer than the GaAs bandgap, and agree well with experimental measurement results. From the simulated external quantum

efficiency (E.Q.E.) under different incident angles, we predict that the TiO_2 nanostructured ARC is able to achieve substantial increases in the longer-wavelength photocurrent response at oblique incident conditions due to the improved coupling to optical guided modes for off-normal incidence conditions, which could find promising photovoltaic applications where light is expected to be incident on the device surface over a wide range of incident angles.

2.2.1 The concept of light trapping

In order to meet the growing global photovoltaic demand, efforts have been made to further increase the efficiency while reducing the cost of photovoltaic cells. One of the approaches that have recently emerged for reducing the cell cost is by employing thin-film solar cells separated from their epitaxial growth substrate, which can then be re-used, via various strategies such as the epitaxial-lift off technique. At the same time, thin-film solar cells possess other advantages such as light weight, structural flexibility, and ease of integration with different photovoltaic setups. [41, 42] However, as the cell thickness becomes thinner, light absorption in solar cells is reduced, particularly at longer wavelengths. As a consequence, in order to help fulfill today's global demand for photovoltaic energy generation, people adopt light trapping technology, which is an effective method for overcoming the problem of insufficient optical absorption in thin-film solar cells.

The basic idea for light trapping is to create additional micro- [43] or nano-scale structures [44] on the front or back surface of the thin-film solar cell which manipulate the direction of the incident light such that the optical path length of the incident light inside the thin-film solar cell device layer can be substantially increased, e.g. using

periodic photonic structures to couple the incident light into optical guided modes, leading to increased optical absorption. Figure 2.2 shows a schematic diagram of a thin-film cell device integrated with backscattering nanostructures such that the incident light can be coupled into different optical waveguide modes inside the device layer.

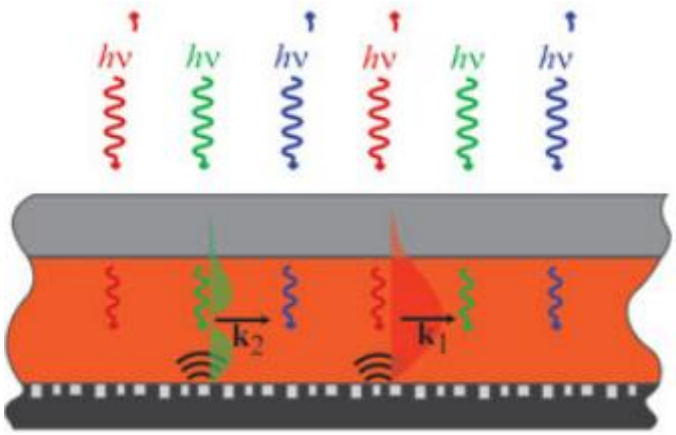

Figure 2.2. Schematic diagram of a backscattering nanostructure implemented in the thin-film photovoltaic device. Incident light is scattered into optical waveguide modes, labeled k_1 and k_2 in the figure. [45]

2.2.2 Sample growth and fabrication process

Samples for these studies were grown by solid-source molecular beam epitaxy (MBE) on GaAs (001) n-type substrates with the structure shown schematically in Figure 2.3(a). A 300nm n-type ($n \sim 2.5\times10^{18}cm^{-3}$) $Al_{0.85}Ga_{0.15}As$ sacrificial layer was grown initially, followed by a 200nm n-type ($n \sim 2.0\times10^{18}cm^{-3}$) GaAs emitter layer. The undoped intrinsic region was grown afterwards, and consisted of three 4nm $In_{0.3}Ga_{0.7}As$ quantum wells (QWs) separated by 17nm GaAs barriers with 21nm GaAs spacer layers grown above and below the QW region. Growth of a 1500nm p-type ($p \sim 5.0\times10^{18}cm^{-3}$) GaAs base layer and a finally a 20nm p^+ ($p \sim 5.0\times10^{19}cm^{-3}$) GaAs contact layer finished the epitaxial layer structure. Throughout each growth, the temperature was kept above 500 ^oC.

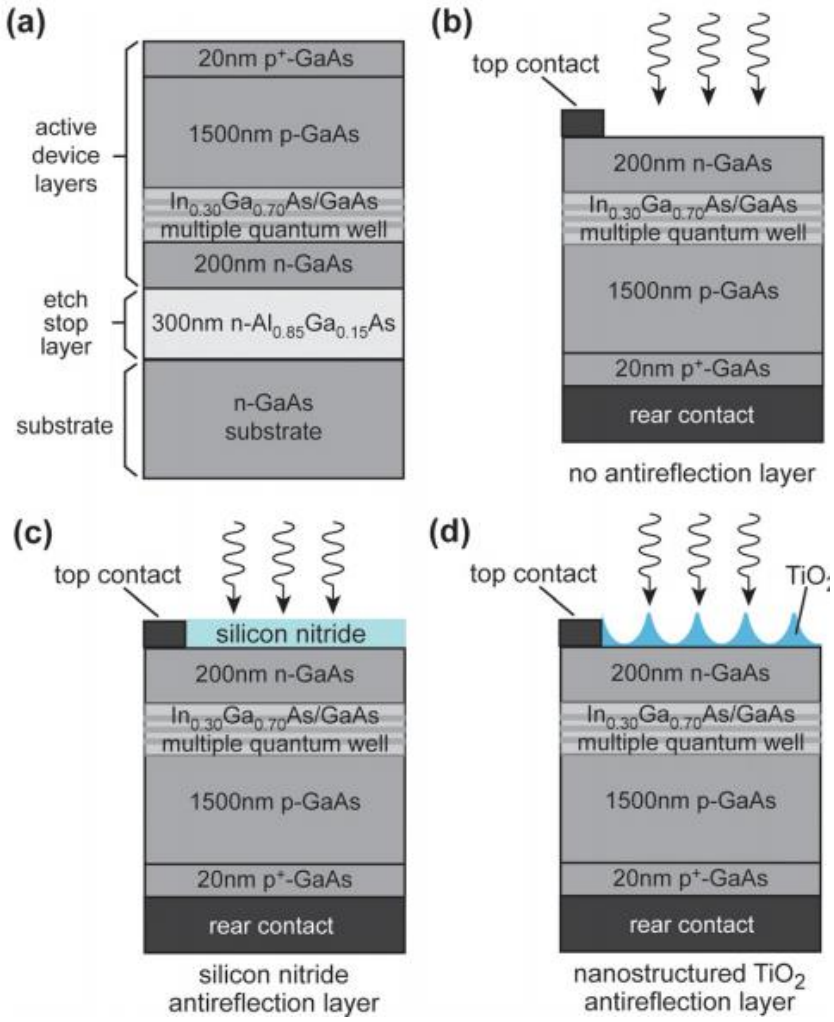

Figure 2.3. (a) Schematic diagram of epitaxial layer structures for the GaAs/$In_{0.3}Ga_{0.7}As$ QW solar cell structure. (b)-(d) Schematic diagrams of final QW solar cell device structures fabricated without ARC layer (b), with silicon nitride thin-film ARC (c), and with nanostructured TiO_2 ARC (d).

Completed device structures labeled in Figure 2.3 (b)-(d) were fabricated through a flip-bond process, and followed by a substrate removal process as shown in Figure 2.5(a). 10nm Cr/100nm Au/1200nm In metallization and 10nm Ti/800nm Au metallization were deposited onto the p^+ GaAs contact layer surface and the silicon substrate, respectively. Then, the metallized two surfaces were pressed together using a home-made wafer-bonding apparatus, as shown in Figure 2.4, at 180^{o}C for 20min. After

the bonding process, with the cell edges covered with black wax to prevent lateral etching, the substrate was removed by wet etching in $NH_4OH:H_2O_2$ (1:19) followed by 50% citric acid: H_2O_2 (4:1)， [46] with the etching solution composition chosen to maximize the etching rate of the GaAs substrate and the selectivity between the $Al_{0.85}Ga_{0.15}As$ sacrificial layer and semiconductor device layers, respectively. After the substrate removal process, the $Al_{0.85}Ga_{0.15}As$ sacrificial layer was removed using 10% diluted hydrofluoric acid. Finally, 1mm × 1mm device mesas were completed by photo lithography patterning, followed by wet etching in $NH_4OH:H_2O_2$ (1:19).

For devices with a conventional single-layer thin-film ARC, 76nm silicon nitride was deposited onto the device surface using e-beam evaporation, and the top n-type contact layer was created by e-beam evaporation of 25nm AuGe/10nm Ni/100nm Au. For

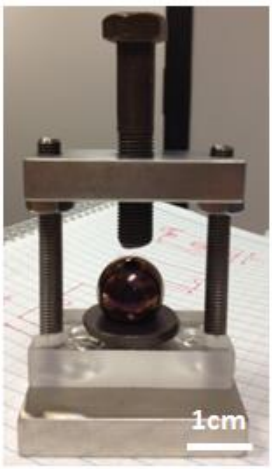

Figure 2.4. A photograph of the home-made wafer-bonding apparatus.

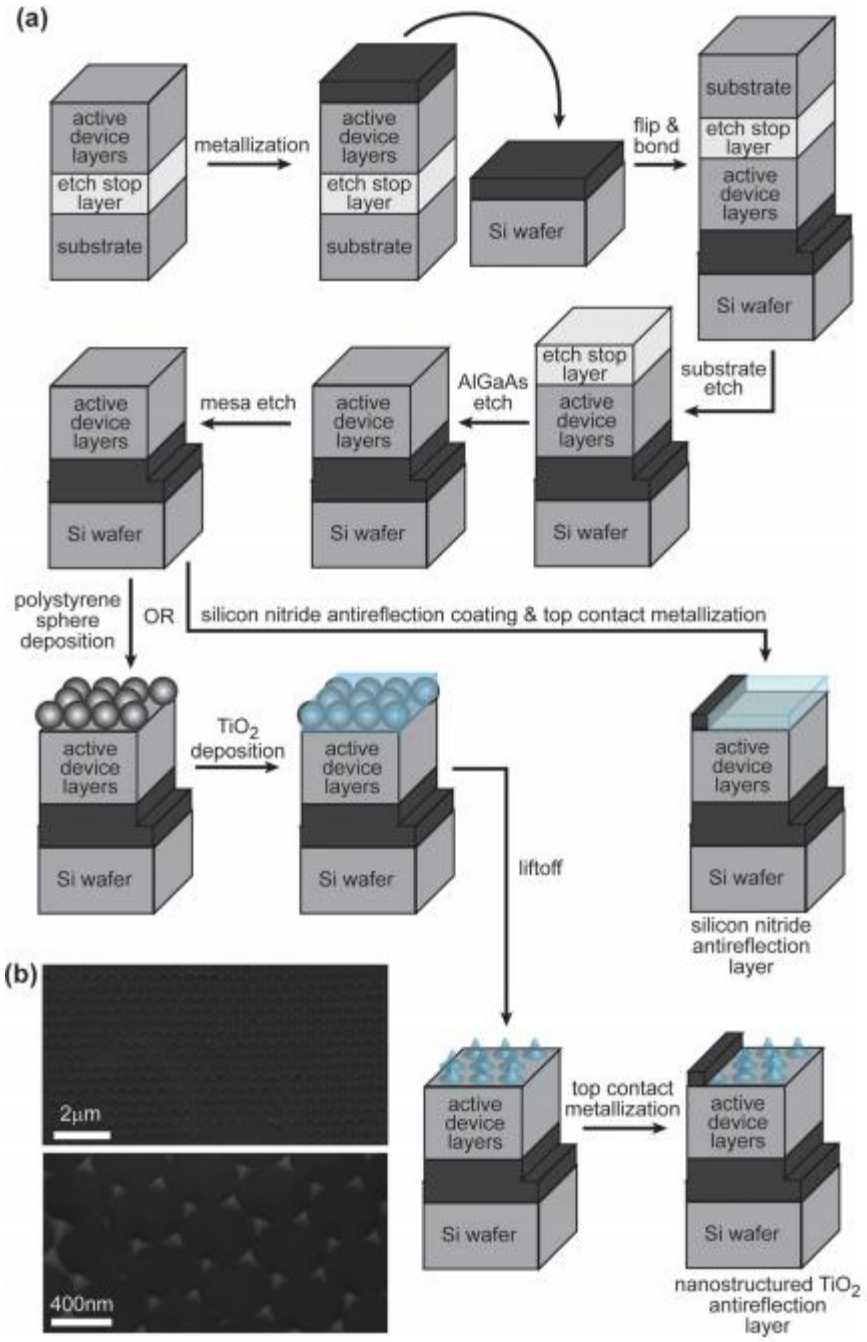

Figure 2.5. (a) Process flow for fabrication of thin-film solar cell devices with either single layer silicon nitride ARC or nanostructured TiO_2 ARC. (b) Scanning electron microscopy (SEM) images of nanostructured TiO_2 ARC on GaAs surface.

devices with a nanostructured TiO_2 ARC, 500nm diameter polystyrene spheres were deposited onto the SiO_2 surface using a Langmuir-Blodgett process, [47] forming a

monolayer hexagonal array sphere mask. Then 250nm TiO_2 was deposited using e-beam evaporation followed by a lift-off process consisting of sonication in toluene solution for 3s. The n-type metallic contact deposition process was the same as discussed above. The resulting TiO_2 nanostructured ARC can be seen in the SEM images as shown in Figure 2.5(b).

2.2.3 Fabry-Perot resonances and optical guided modes

Figure 2.6(a) shows the current-voltage characteristics measured under AM1.5G 1-sun illumination for devices with no ARC (grey), with a conventional single-layer silicon nitride thin-film ARC (red), and with a nanostructured TiO_2 ARC (blue), respectively. The nanostructured TiO_2 ARC yields the highest short-circuit current density, J_{sc} ~ 14.62mA/cm^2, compared to the conventional single-layer silicon nitride ARC (J_{sc} ~ 13.82mA/cm^2) and the reference device without an ARC (J_{sc} ~ 9.52mA/cm^2). The superior antireflection performance of the nanostructured TiO_2 ARC compared to the conventional single-layer silicon nitride ARC is attributed to the "nanopyramid" shape of TiO_2 nanostructures, which leads to a gradual change in the effective refractive index from the incident medium (air) to the GaAs surface. Approaches of employing structures that have a "graded" refractive index profile to achieve antireflection performance over a broad range of wavelengths have been extensively studied. [48-50] In this study, we focus on the light trapping property of nanostructured TiO_2 ARC which couples the incident light into optical guided modes within the solar cell device layer, leading to increased longer-wavelength optical absorption.

The measured and numerically simulated E.Q.E. shown in Figure 2.6(b) provides more detailed comparison for ARCs of each type. As expected, in both simulated and measured results, the device with no ARC exhibits much lower E.Q.E. compared to devices with the single-layer silicon nitride thin-film ARC, and the nanostructured TiO_2 ARC. At wavelengths shorter than ~ 600nm, the measured E.Q.E. is substantially higher for the device with the nanostructured TiO_2 ARC compared to the device with the single-layer silicon nitride thin-film ARC, which is consistent with the simulation results. For wavelengths between ~ 600nm and ~ 820nm, both types of ARCs show similar antireflection performance, while at wavelengths longer than ~ 820nm, the measured and simulated E.Q.E. for the device with nanostructured TiO_2 ARC exhibit the highest value. In addition, because of the fact that surface recombination is neglected in the simulation, we attribute the differences between the simulated and measured E.Q.E. spectra at wavelengths shorter than the GaAs bandgap at ~ 850nm to the nonradiative surface recombination velocity of ~ 10^6cm/s, a reasonable estimation given the device surface dopant concentration of 2.5×10^{18}cm^{-3}. [51] At wavelengths between 700nm and 850nm, we observe oscillations in both simulated and measured E.Q.E. spectra, which arise from Fabry-Perot resonances for wavelengths at which the thin-film device layer thickness is shorter than the absorption depth.

We then focus on simulated and measured E.Q.E. spectra peaks at wavelengths longer than ~ 900nm, where absorption occurs primarily in the GaAs/$In_{0.3}Ga_{0.7}As$ QWs. In this wavelength range, peaks observed for the device with no ARC and with the single-layer silicon nitride thin-film ARC are indistinguishable. Peaks observed at wavelengths of 930nm, 990nm, and 1060nm in the measured spectra and at wavelengths of 920nm,

970nm, and 1030nm in the simulation results arise from Fabry-Perot resonances in the thin-film device layer. Similar behavior can be found in a previous report for studying light trapping in QW solar cells grown on distributed Bragg reflector multilayers. [30] For the device with the nanostructured TiO_2 ARC, significantly different behavior is observed in this wavelength range. In addition to peaks observed in the simulated spectrum at 920nm, 970nm, and 1030nm, the same as those observed for devices with no ARC and with single-layer silicon nitride thin-film ARC, we also observe peaks at 900nm, 940nm, and 990nm. In order to analyze the physical origin of these peaks, we simulated electric field distributions for light polarized along the *y* direction impinging on QW devices with either a single-layer silicon nitride thin-film ARC or a nanostructured TiO_2 ARC at wavelengths of 970nm and 990nm, as shown in Figure 2.7. At 970nm, shown in Figure 2.7(c), the electric field in the device layer is observed to be predominantly along the *y* direction for both types of ARCs, indicating that at this wavelength, the peak observed in the E.Q.E. spectra is associated with a Fabry-Perot resonance. Similar analyses imply that simulated E.Q.E. peaks at 920nm and 1030nm for both devices are associated with Fabry-Perot resonances. As shown in Figure 2.7(d), at 990nm, the simulated electric field in the device layer for the nanostructured TiO_2 ARC is primarily polarized along the *z* direction, indicating that at this wavelength, the incident light is coupled into an optical guide mode by the nanostructured TiO_2 ARC, leading to a large enhancement in QW absorption. Similar analyses confirm that simulated E.Q.E. peaks at 900nm and 940nm arise from similar coupling behavior. In the measured E.Q.E. spectrum for the device with the nanostructured TiO_2 ARC, we observe two closely spaced peaks at 930nm – 950nm, which is interpreted as corresponding to a combination

of Fabry-Perot and optical guided mode peaks at 920nm and 940nm in the simulated spectrum. A similar interpretation can be applied to measured E.Q.E. peaks at 990nm and 1070nm. In addition, compared to simulated spectra, the measured peaks are generally lower in amplitude but broader in width, which we attribute to differences in arising from fabrication-induced variations in actual devices.

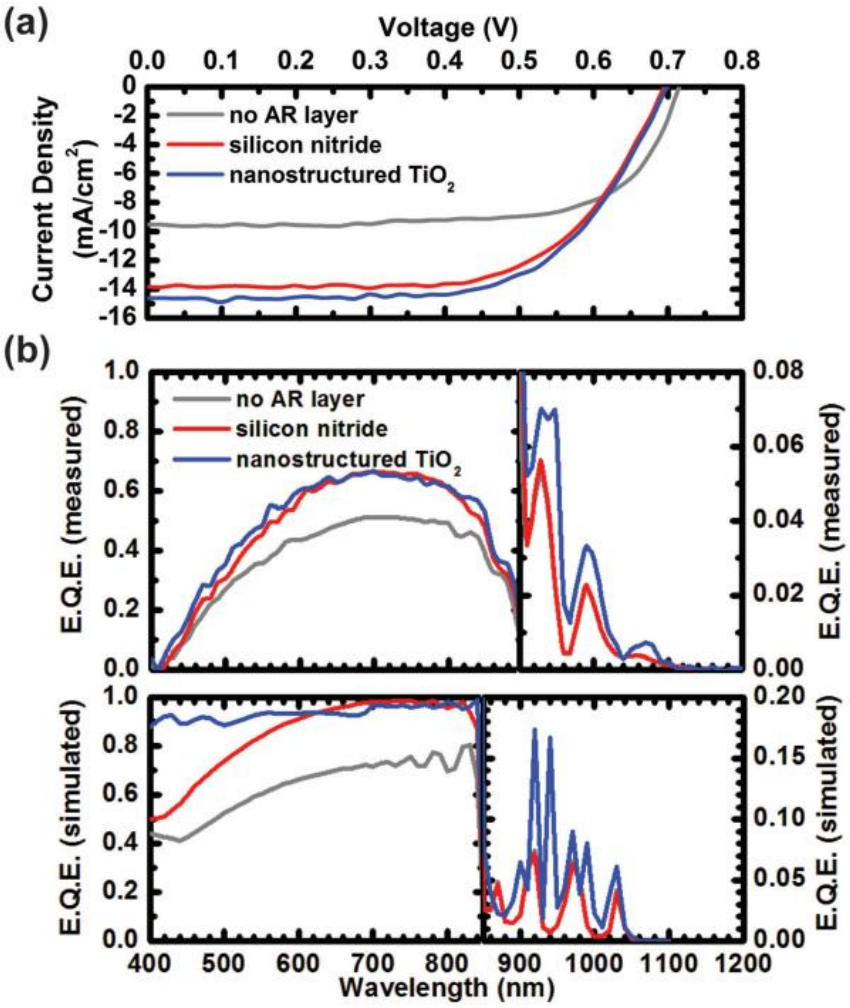

Figure 2.6. (a) Current-voltage characteristics for each device measured under AM1.5G 1-sun illumination from a solar simulator. (b) Measurement and numerical simulation results of E.Q.E. for devices of each type.

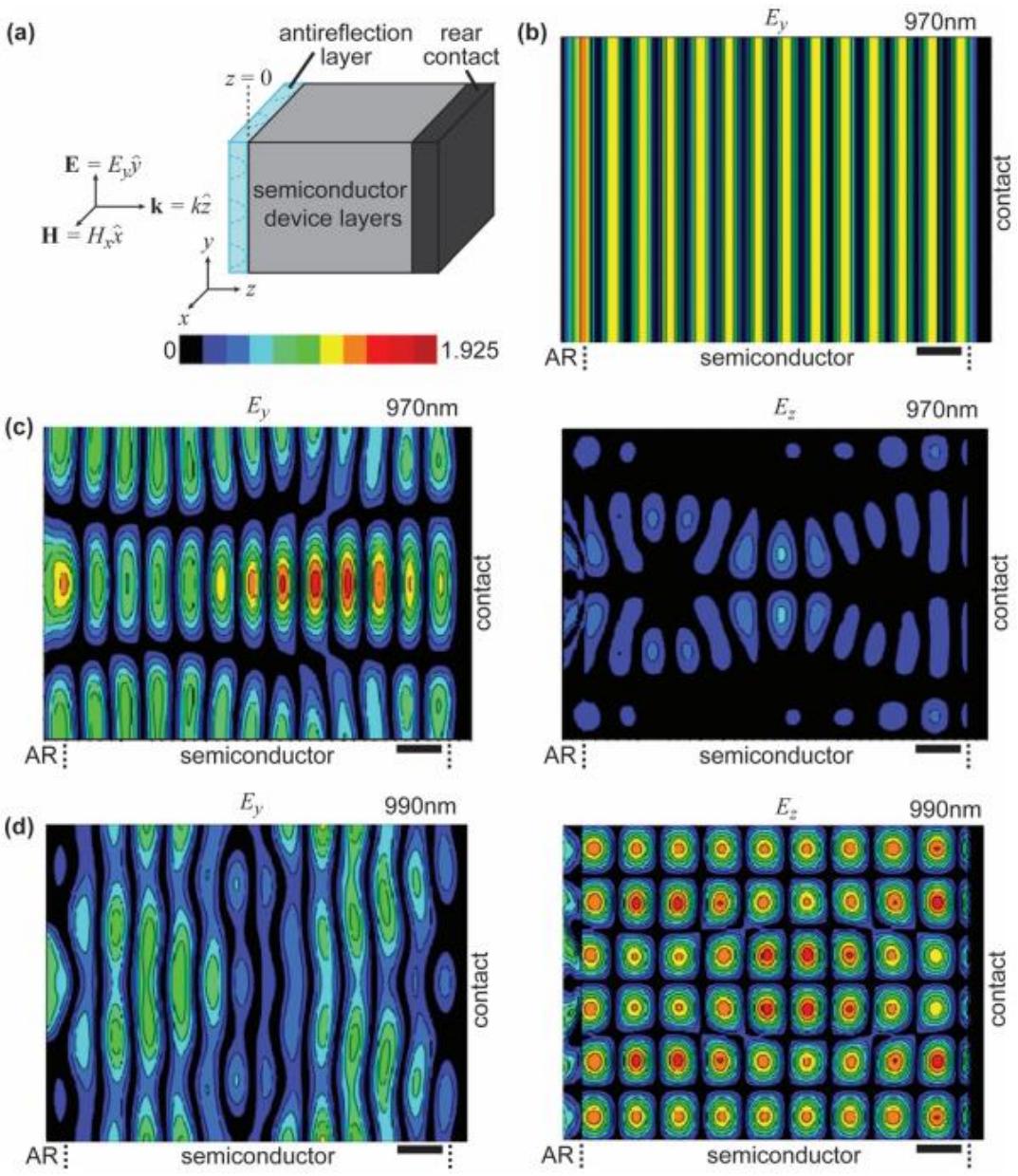

Figure 2.7. (a) Schematic diagram of the incident field and the device geometry for simulations. (b)-(d) Plots of simulated electric field distributions for light incident on GaAs/$In_{0.3}Ga_{0.7}As$ QW solar cell device with either single-layer silicon nitride thin-film ARC or nanostructured TiO_2 ARC at wavelengths of 970nm and 990nm, with incident light polarized along the *y* direction. (b) E_y at 970nm for the device with silicon nitride; (c) E_y and E_z at 970nm for the device with nanostructured TiO_2; (d) E_y and E_z at 990nm for the device with nanostructured TiO_2. Scale bar for all plots is 200nm.

2.2.4 Broad-spectrum, wide-angle antireflection performance

The nanostructured TiO_2 antireflection coating is also expected to provide low surface reflectance over broad ranges of incident angles and wavelengths. Figure 2.8 shows numerically simulated photocurrent response spectra for the QW cell with a conventional single-layer silicon nitride antireflection coating and the cell with a TiO_2 nanostructured antireflection coating for light incident at angles of 20^o, 40^o, and 60^o, while the simulated photocurrent response spectra at normal incidence is shown in Figure 2.6(b). The incident light is taken to be 45^o-polarized, which includes s-polarized and p-polarized components with equal amplitudes.

It is observed that for both structures, the simulated photocurrent response changes little with the varying incident angle for wavelengths shorter than the GaAs band edge at ~850nm. For the structure with the single-layer silicon nitride antireflection coating, this occurs because the increased reflectance for the s-polarized component with increasing incident angle is cancelled by the decreased reflectance for p-polarized light as the incident angle approaches Brewster's angle. For wavelengths shorter than ~600nm, the cell with the TiO_2 nanostructured layer yields increased photocurrent response compared to the cell with the single-layer silicon nitride antireflection coating from normal to 60^o angle of incidence. For wavelengths between ~600nm and ~850nm, both structures yield similar levels of photocurrent response over the entire range of incident angles. For wavelengths longer than ~850nm, where photon absorption occurs primarily in the QW region, peaks in the photocurrent response spectrum for the cell with the single-layer silicon nitride antireflection coating associated with each Fabry-Perot resonance yield a shift to shorter wavelength and little change in magnitudes. For the cell

with TiO_2 nanostructured layer, a substantial increase in photocurrent response at wavelengths longer than ~850nm is observed compared to that of normal incidence due to the improved coupling of incident light into optical guided modes at off-normal incident conditions. This observation suggests that such approaches can be promising in photovoltaic applications where sunlight energy harvesting over a broad range of incident angles is desired.

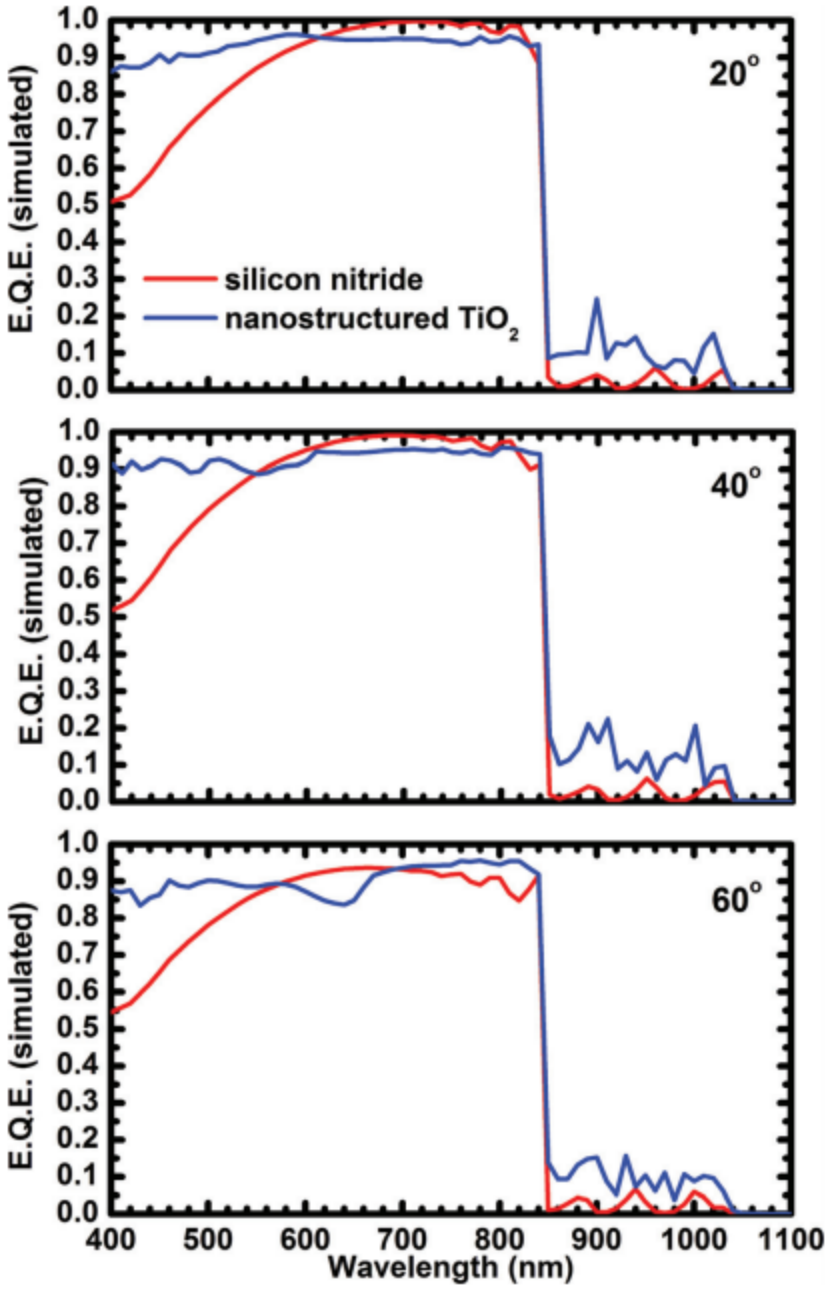

Figure 2.8. Simulated external quantum efficiency (E.Q.E.) for device structures with silicon nitride thin-film antireflection coating (red) or nanostructured TiO_2 antireflection layer (blue), as functions of wavelength and computed for incident angles polarization at the midpoint (45^o) between s-polarization and p-polarization.

2.2.5 Conclusion

In conclusion, we have analyzed thin-film GaAs/$In_{0.3}Ga_{0.7}As$ QW solar cells with a single-layer silicon nitride thin-film ARC, and with a nanostructured TiO_2 ARC via both numerical simulations and experimental measurements. We observe that the nanostructured TiO_2 ARC not only shows superior antireflection performance compared to that of conventional single-layer silicon nitride ARC, but also scatters the incident light into optical guided modes inside the thin-film solar cell device layer. Measurement results show that the thin-film QW solar cell with the nanostructured TiO_2 ARC yields ~ 5.8% increase in J_{sc} compared to the same device but with a conventional single-layer silicon nitride thin-film ARC. In addition, by examining the electric field distribution plots for incident light longer than ~ 900nm, where absorption primarily occurs in the QW region, we can elucidate each E.Q.E. peak is associated with either Fabry-Perot resonance or optical guided modes within the thin-film QW solar cell device layer. Furthermore, simulated photocurrent response spectra at off-normal incident conditions suggest that this approach can benefit a variety of photovoltaic systems where light harvesting over a broad range of incident angles is desired.

2.3 BACK SIDE LIGHT TRAPPING SCATTERING STRUCTURES

In section 2.3, we discuss the numerical simulation, fabrication, and measurement results of GaAs/$In_{0.3}Ga_{0.7}As$ QW thin-film solar cell with nanostructured metal/dielectric rear contacts. We focus on analyzing the angular dependence of light trapping effects associated with these structures. The roles of Fabry-Perot resonances and guided optical modes within the thin-film device layer are numerically and experimentally analyzed at incident angles from 0^o to 30^o, and good agreement is found between simulation and measurement results. We show that with the nanostructured rear contacts, E.Q.E. of longer wavelengths can reach as high as 2.9% per QW, significantly exceeding the ~ 1% per QW level which is typically observed.

2.3.1 Sample growth and fabrication process

We use the same set of samples studied in section 2.2, and detailed schematic diagrams of the GaAs homojunction and GaAs/$In_{0.3}Ga_{0.7}As$ QW solar cell structures are shown in Figure 2.9. For devices with planar metallic rear contacts, we employ a similar "flip bond" fabrication process as discussed in section 2.1 for transferring thin-film solar cell devices onto pre-metallized rigid silicon substrates with details shown in Figure 2.10(a). 10nm Cr/40nm Au/1200nm In was evaporated onto the p^+ GaAs surface, and 10nm Ti/800nm Au was evaporated onto the silicon substrate surface, respectively. Then, we used the home-made wafer-bonding apparatus shown in Figure 2.4 to press the two surfaces tightly together under the ambient temperature of 180^oC for 20min. The GaAs substrate was removed by wet etching in $NH_4OH:H_2O_2$ (1:19) followed by 50% citric acid:H_2O_2 (4:1). A photolithography process followed by wet etching in $NH_4OH:H_2O_2$

(1:19) resulted in device mesas of 1 × 1mm^2 and 2 × 2mm^2. Finally, similar n-type AuGe/Ni/Au metallic contacts were deposited by e-beam evaporation.

For devices with nanostructured metal/dielectric rear contacts, prior to metallization on the p^+ GaAs surface, 80nm SiO_2 was deposited using e-beam evaporation. Then, as shown in Figure 2.10(b), 500nm diameter polystyrene spheres were deposited onto the SiO_2 surface using a Langmuir-Blodgett process, resulting in a hexagonal sphere array for patterning by nanosphere lithography (NSL). An oxygen plasma etch was used to reduce the sphere diameter, followed by deposition of 15nm Cr, and a lift-off process in which the polystyrene spheres were removed in toluene solution under sonication, and SiO_2 was reactive ion etched in a gas mixture of CF_4/O_2. Finally, 10nm Cr/40nm Au/1200nm In metallization was deposited, forming the metal/dielectric nanostructured rear contact. The remainder of the fabrication process was the same with that of the thin-film solar cell device with planar metallic contacts. Figure 2.10(c) shows an SEM image of 500nm diameter polystyrene spheres deposited onto the SiO_2 surface by NSL, and an atomic force micrograph of an etched hole array in SiO_2 prior to metallization. The schematic diagrams of the resulting devices of each type are shown in Figure 2.11.

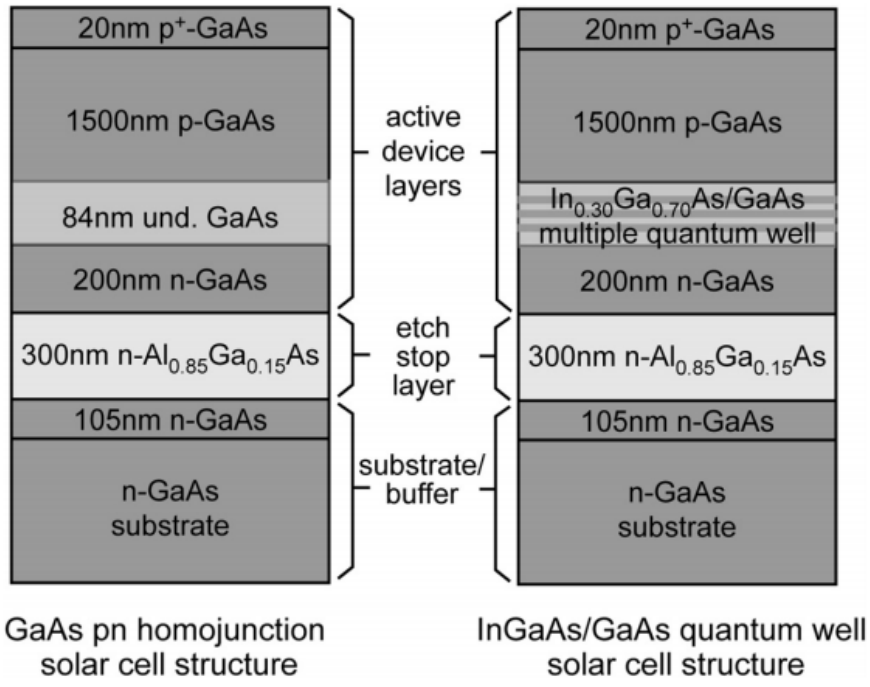

Figure 2.9. Schematic diagrams of epitaxial layer structures for (left) GaAs homojunction solar cell structure, and (right) GaAs/$In_{0.3}Ga_{0.7}As$ QW solar cell structure. Labels of active device layers, etch stop layer, and substrate buffer correspond to sample layers labeled in Figure 2.8.

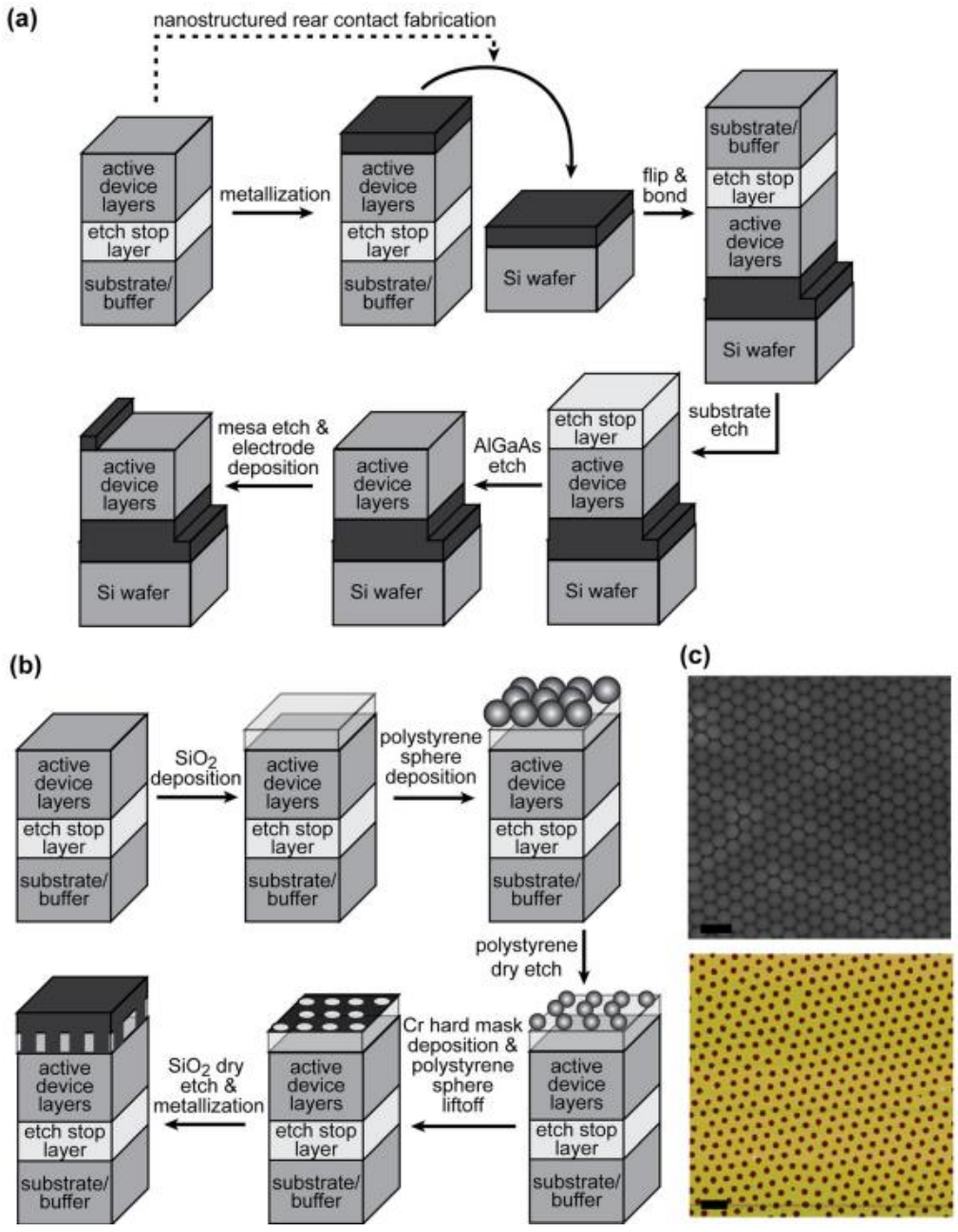

Figure 2.10. (a) Process flow for key steps in the "flip-bond" layer-transfer fabrication of thin-film solar cell structures with a planar metallic rear contact. (b) Additional steps for fabrication of thin-film solar cell structures with nanostructured metal/dielectric rear contacts using NSL, which are incorporated into the complete fabrication process flow in (a) as indicated by the dashed line. (c) SEM image of a hexagonal array of 500nm diameter polystyrene spheres deposited using NSL (top), and atomic force microscopy image of etched hole array in SiO_2 layer prior to metallic contact deposition (bottom). Scale bars are 1 μm for both images.

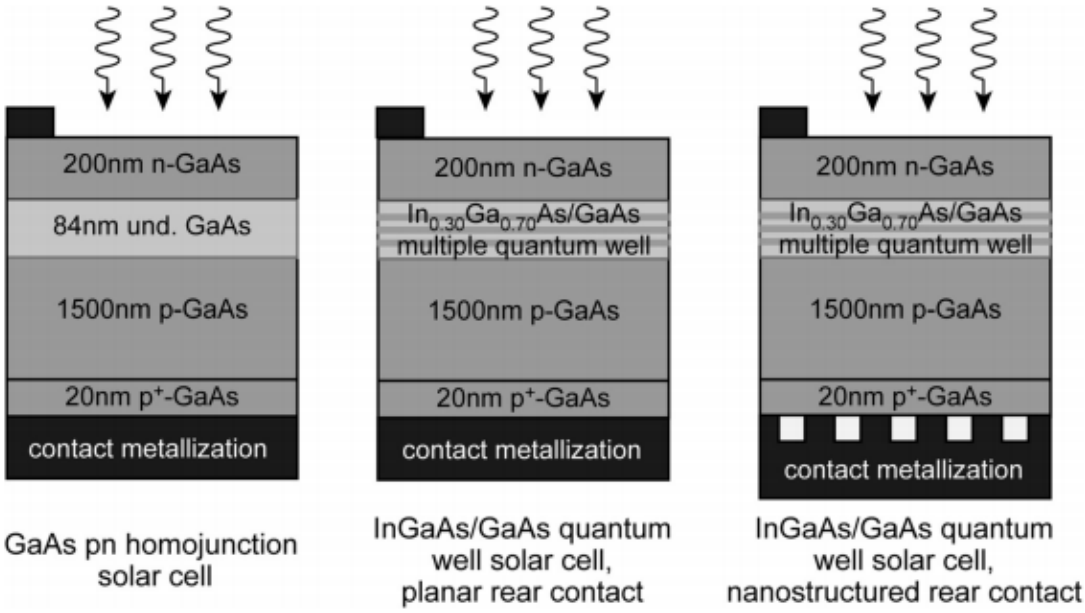

Figure 2.11. Schematic diagrams of GaAs homojunction solar cell device, GaAs/$In_{0.3}Ga_{0.7}As$ QW solar cell device with planar metallic rear contacts, and GaAs/$In_{0.3}Ga_{0.7}As$ QW solar cell device with nanostructured metal/dielectric rear contact.

2.3.2 Angular dependence of light trapping mechanisms

Figure 2.12(a) shows measured current-voltage characteristics for all three device types. The GaAs/$In_{0.3}Ga_{0.7}As$ QW solar cell with the nanostructured metal/dielectric rear contact yields the highest J_{sc} (10.18mA/cm^2), compared to the QW cell (9.52mA/cm^2) and the homojunction cell (8.68mA/cm^2) with planar metallic rear contacts. Figure 2.12(b), (c) show measured and simulated E.Q.E. for devices of each type. For wavelengths shorter than the GaAs bandgap at ~900nm, E.Q.E. for all three device types are similar as expected. For wavelengths longer than ~900nm, where absorption primarily occurs in the QW region, specific peaks in the photocurrent response spectra can be observed, which are associated with either Fabry-Perot resonance or guided optical modes as analyzed in section 2.2. In a similar way, we analyzed the physical mechanisms of the photocurrent response enhancement, particularly at the longer

wavelength range. Shown in Figure 2.13 are simulation results of electric field distributions inside the device layer for *y*-polarized incident light at wavelengths of 970nm and 990nm. At 970nm, electric field distributions for both device types are primarily along the *y* direction, indicating that at this wavelength, the simulated E.Q.E. peak in the spectrum is predominantly associated with a Fabry-Perot resonance. We conclude based on similar analysis that for both device types, E.Q.E. peaks at 870nm, 920nm, and 1030nm arise from Fabry-Perot resonance. At 990nm, it is observed that the electric field distribution inside the device layer is predominantly along the *z* direction as shown in Figure 2.13(b), indicating that the incident light at this wavelength is strongly coupled into an optical guided mode inside the device layer, propagating in the direction orthogonal to that of the incident light. Deriving from a similar analysis we conclude that E.Q.E. peaks at wavelengths of 890nm and 940nm arise from strong coupling into optical modes. For the QW solar cell device with planar metallic rear contact, the measured E.Q.E. peaks located at 930nm, 990nm, and 1050nm correspond to simulated E.Q.E. peaks at 920nm, 970nm, and 1030nm. The shifts in E.Q.E. peak positions between measurement and simulation results are due to small differences in simulated and fabricated device structures. Through similar analysis, it is confirmed that measured E.Q.E. peaks at wavelengths of 930nm, 980nm, and 1040nm correspond to combinations of closely spaced Fabry-Perot and guided-mode peaks at 920nm-940nm, 970nm-990nm, and 1030nm-1050nm in the simulated E.Q.E.

In order to further analyze the light trapping mechanisms under oblique incident angle conditions, we simulated and measured E.Q.E. spectra for the QW solar cell device with the nanostructured rear contact under incident angles from 0^o to 30^o as shown in

Figure 2.14. It is observed that peaks at the longer wavelength range (> 900nm) in measured and simulated E.Q.E. spectra shift slightly with the increasing incident angle. This phenomenon can be explained by mode dispersion relations derived from Bragg coupling equations [44, 52] which will be discussed in more detail below.

Figure 2.15 shows simulated electric field distributions inside the nanostructured rear contact-integrated QW solar cell device layer with the incident light polarized along the *y*-direction at 10^{o} off-normal incidence for wavelengths of 960nm and 990nm (a)-(d), and the simulated E.Q.E. spectrum at 10^{o} off-normal incidence. From an analysis of field distribution plots similar to that described above, we conclude that at 960nm, the enhancement in the simulated E.Q.E. spectrum is predominantly associated with mode coupling effect; while at 990nm, the enhancement in the simulated E.Q.E. spectrum is predominantly associated with Fabry-Perot resonance. Similar analysis also applies to E.Q.E. spectra under different incident angles, which reveals the angular dependence of Fabry-Perot resonances and coupling to optical guided modes for the QW device with nanostructured rear contact. The derived angular dependences are summarized in Figure 2.16. Good agreement is found comparing the simulated peak wavelengths with calculated mode dispersion. For wavelengths shorter than ~900nm, the simulated and measured E.Q.E. curves have little change with the increasing incident angle because the decrease in transmittance for TE-polarized light is cancelled by the increase in transmittance for TM-polarized light when approaching the Brewster's angle. [53] For wavelengths longer than ~900nm, we do not observe significant degradation in E.Q.E. with the increasing incident angles, which can be explained by the increased number of allowed waveguide modes at off-normal incidence as deduced from the Bragg coupling

condition. Hence, our proposed light trapping strategy is demonstrated to be able to provide angle-robust antireflection performance, and can potentially find application in various photovoltaic systems, particularly in those where light impinging on the cell surface over a wide range of incident angles such as concentrating photovoltaics and non-tracking solar systems.

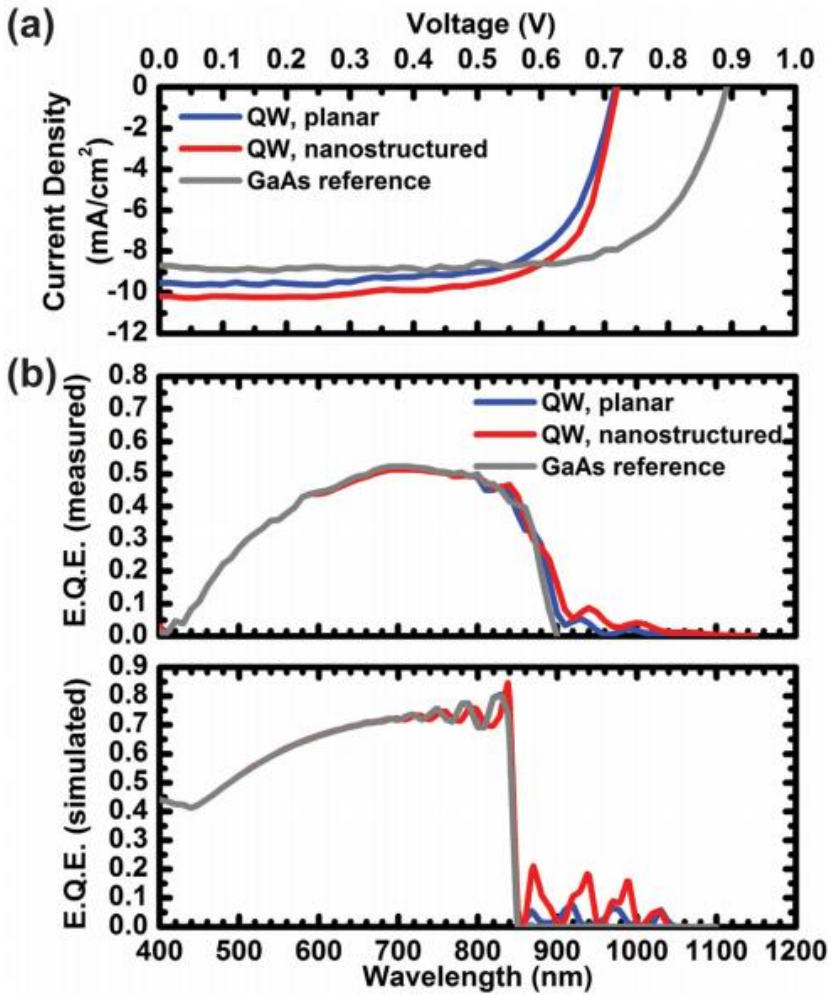

Figure 2.12. (a) Current density-voltage characteristics measured under AM1.5G 1sun illumination for solar cell devices of each type. (b) Measured and simulated E.Q.E. spectra for all three device types.

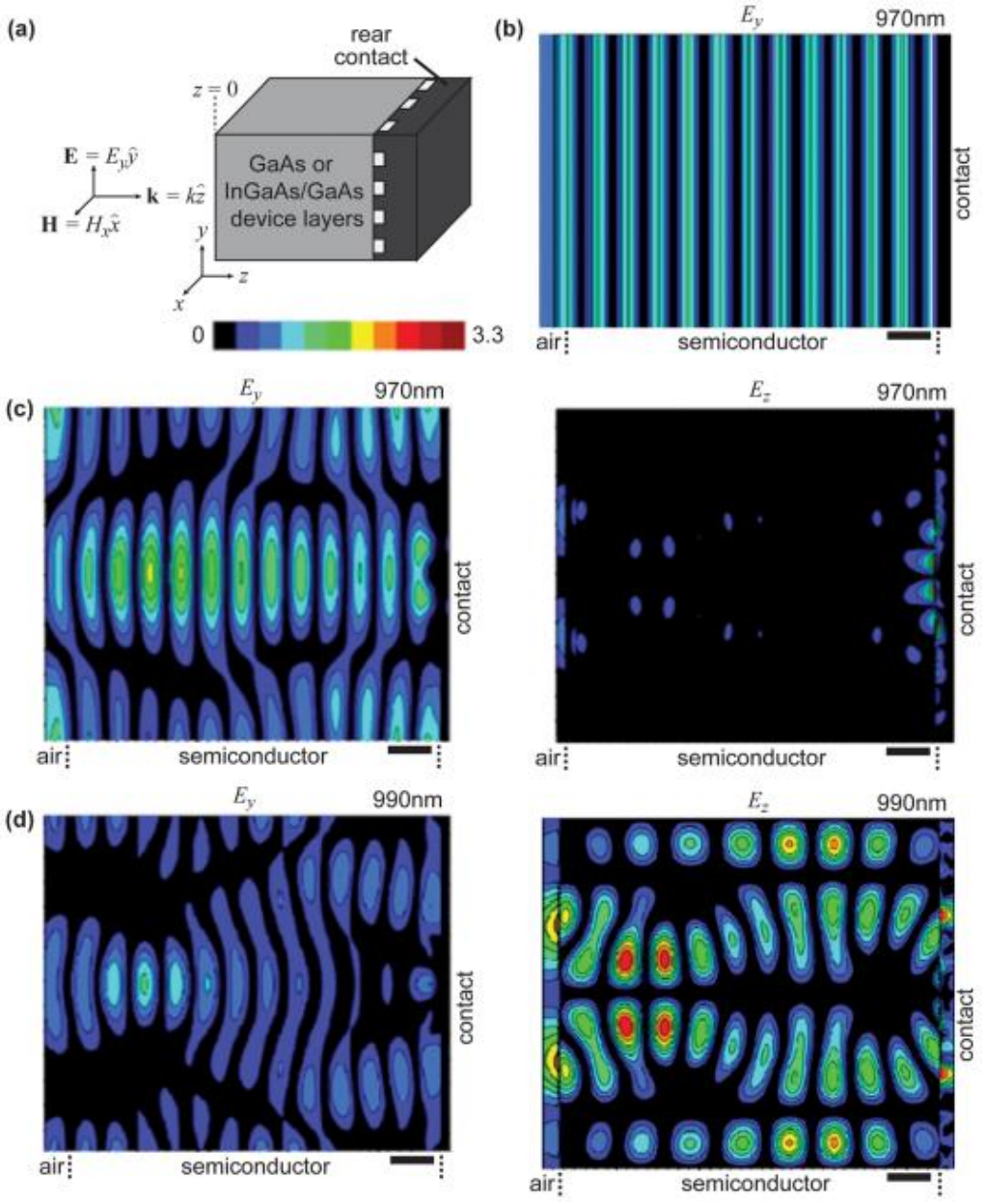

Figure 2.13. (a) Schematic diagram of the incident field and the device geometry. (b)-(d) Plots of electric field distributions simulated for the incident wavelength of 970mn and 990nm for GaAs/$In_{0.3}Ga_{0.7}As$ QW solar cell devices with either planar or nanostructured rear contacts.

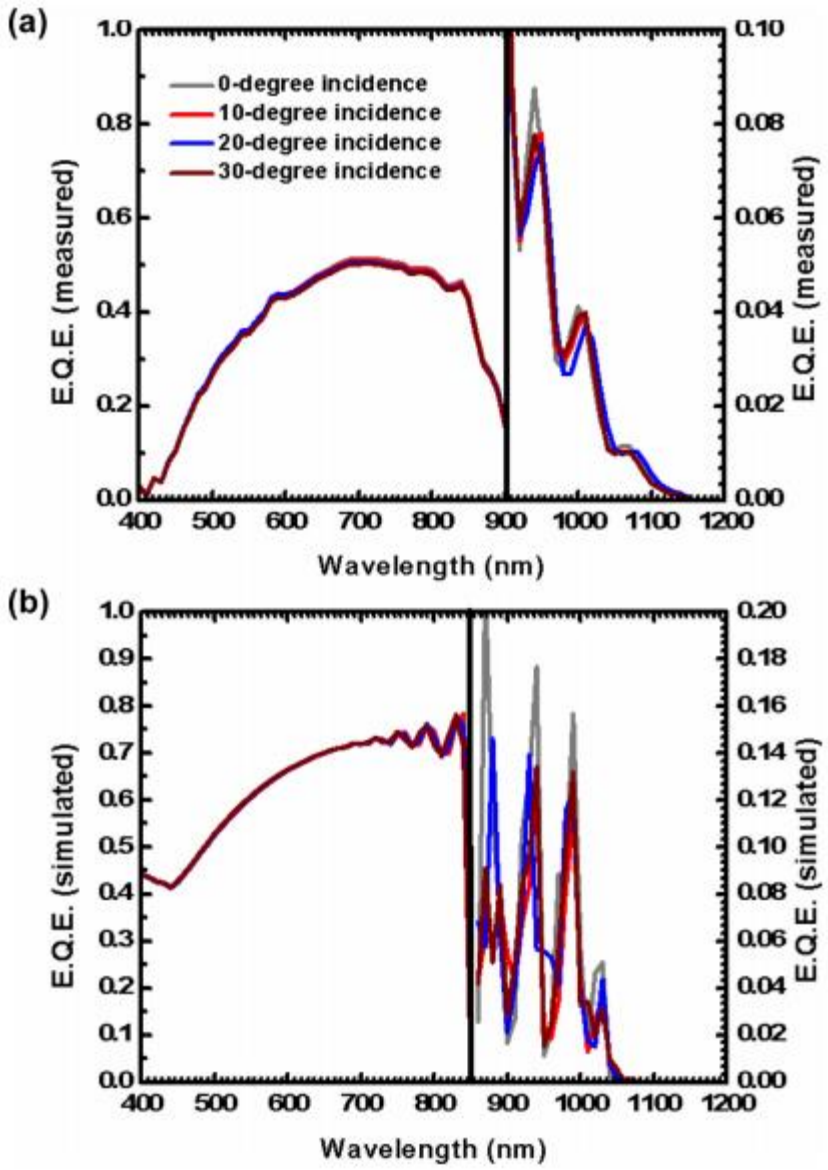

Figure 2.14. (a) Measured and (b) simulated photocurrent response spectra for the GaAs/$In_{0.3}Ga_{0.7}As$ QW solar cell device with nanostructured rear contact under incident angles from 0^o to 30^o.

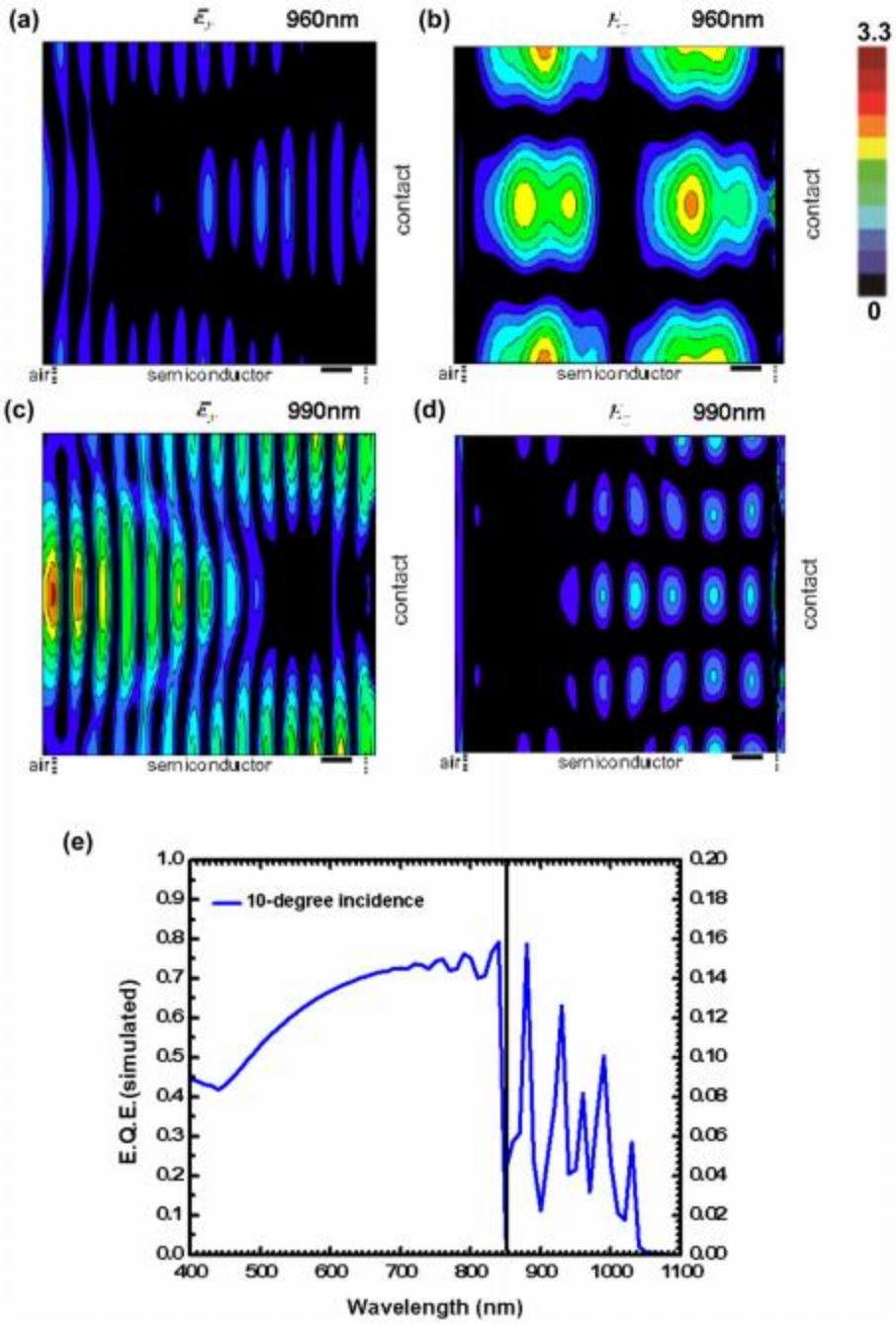

Figure 2.15. (a)-(d) Representative plots of electric field distributions for the *y*-polarized light incident on the GaAs/$In_{0.3}Ga_{0.7}As$ QW solar cell device surface at an angle of 10^o at wavelengths of 960nm and 990nm. (e) Simulated E.Q.E. spectrum for the GaAs/$In_{0.3}Ga_{0.7}As$ QW solar cell device at 10^o of incidence.

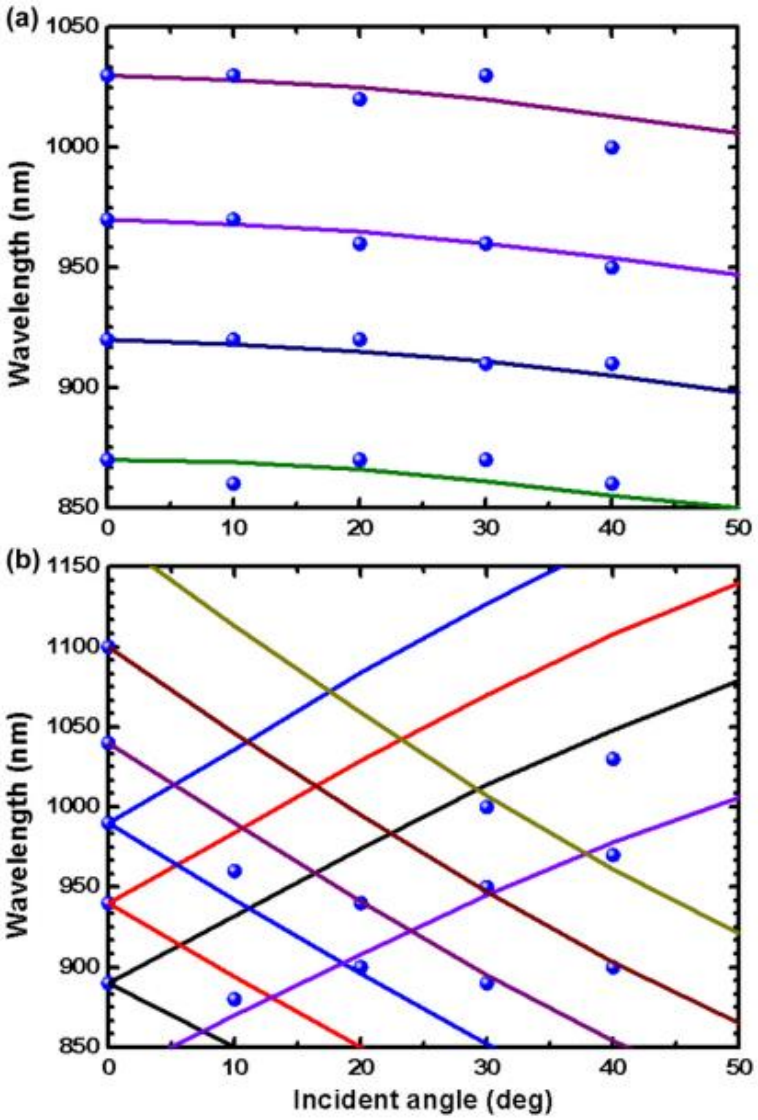

Figure 2.16. Dispersion relations for (a) optical guided modes and (b) Fabry-Perot resonance modes. Symbols correspond to distinguishable peaks in the simulated E.Q.E. spectrum for the GaAs/$In_{0.3}Ga_{0.7}As$ QW solar cell device with incident light polarized along the *y*-direction.

2.3.3 Conclusion

In summary, we have designed, fabricated, and analyzed GaAs/$In_{0.3}Ga_{0.7}As$ QW thin-film solar cells with planar and nanostructured rear contacts. With the integration of the nanostructured rear contact, sub-GaAs bandgap wavelength (> 900nm) absorption can

be substantially increased compared to the cell with planar rear metallic contact. As high as 2.9% per quantum well external quantum efficiency is achieved, significantly surpassing the 1% per quantum well external quantum efficiency typically observed. Light trapping mechanisms of nanostructured rear contacts have been studied under normal and off-normal conditions both numerically and experimentally, and angular dependences of Fabry-Perot resonance modes and optical guided modes have been clearly revealed.

Chapter 3: Integrated Optical Nanostructures on GaAs Solar Cells for Broad-Spectrum, Omnidirectional Improvement of Photovoltaic Performance

3.1 MOTIVATION

A conventional optimized Al_2O_3/TiO_2 bilayer thin-film antireflection coating is able to provide excellent antireflection performance under normal and small incident angles. [54] However, the antireflection performance generally degrades severely at very large incident angles. Figure 3.1 shows the experimental measurement results of transmittance of the conventional Al_2O_3/TiO_2 bilayer thin-film antireflection coating under a coverglass with the incident angle varying from 0^o to 80^o. At smaller incident angles ($< 60^o$), we do not observe obvious degradation in the antireflection performance. Unfortunately, at larger incident angles ($> 60^o$), a significant degradation in the antireflection performance is observed with the increasing incident angle. As a consequence, conventional bilayer thin-film antireflection coating does not meet the demand for most portable and mobile photovoltaic systems where sunlight energy harvesting over a broad range of incident angles is particularly desirable and solar tracking is not feasible. In order to improve the sunlight energy harvesting efficiency for portable and mobile photovoltaic systems, advanced photon management technologies need to be exploited.

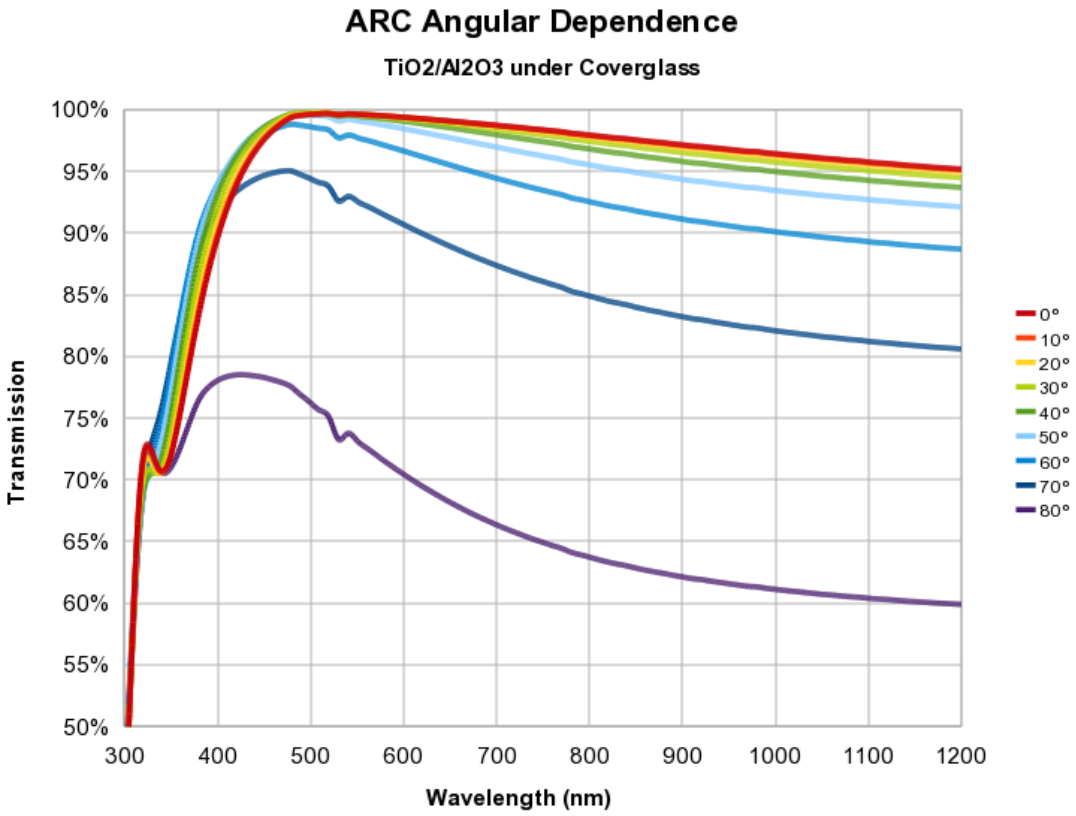

Figure 3.1. Measured transmittance of bilayer Al_2O_3/TiO_2 thin-film antireflection coating under coverglass for different incident angles.

3.2 INTEGRATED OPTICAL NANOSTRUCTURES ON BULK MOCVD-GROWN GAAS SOLAR CELLS FOR BROAD-SPECTRUM, OMNIDIRECTIONAL PHOTOVOLTAIC PERFORMANCE IMPROVEMENT

In section 3.2, taking into account the polymer packaging sheet for real photovoltaic applications, we propose an antireflection strategy based on nanostructures fabricated on surfaces of both the bilayer Al_2O_3/TiO_2 thin-film antireflection coating and the polyethylene terephthalate (PET) packaging sheet patterned via NSL. We demonstrate the optimization process for choosing structural dimensions of the integrated optical nanostructures, and reveal the physical mechanisms for the superior antireflection

performance achieved by such nanostructures. The integrated optical nanostructures are shown to be able to provide improved antireflection performance over wide ranges of incident angles and wavelengths for bulk MOCVD grown GaAs solar cells – Compared to the unpatterned cell, a $1.1\times$ increase in J_{sc}, directly derived from E.Q.E. measurements, is observed for the cell integrated with optical nanostructures at normal incidence, and a $1.67\times$ increase in J_{sc} is observed at 80^{o} angle of incidence. Nanosphere lithography process is shown to provide a rapid, low-cost approach for patterning of subwavelength-scale antireflection structures over cm^2-scale areas.

3.2.1 Experiment

Figure 3.2(a) shows a schematic diagram of a GaAs single-junction solar cell with a conventional Al_2O_3/TiO_2 bilayer thin-film antireflection coating integrated with the Al_2O_3 nanoisland structure and moth-eye textured PET packaging sheet using a space-grade encapsulant, together with the schematic refractive index profile. The Al_2O_3 nanoisland structure and moth-eye textured PET sheet provide gradual transition in refractive indices at each key interface, and are anticipated to be able to provide improved antireflection performance over a wide range of incident angles. For the moth-eye textured PET packaging sheet, 200nm diameter polystyrene spheres were deposited on planar PET sheet surface using NSL, resulting in a hexagonal sphere as a soft mask as shown in Figure 3.2(b). Then, the diameter of the polystyrene sphere array was reduced by reactive-ion etching, with 100sccm of oxygen at a pressure of 200mTorr and radio frequency power of 100W with etching time of 4min, resulting in the moth-eye nanostructure on the PET surface, consisting of arrays of tapered cylindrical pillars of

height ~ 400nm as shown in Figure 3.2(c)-(d). Figure 3.2(e) shows an SEM image of the fabricated moth-eye nanostructure on the PET substrate. Similarly, for the Al_2O_3 nanoisland structure, a 1000nm diameter polystyrene sphere array was deposited on the cell surface employing NSL as shown in Figure 3.2(f), followed by the deposition of 500nm of Al_2O_3 via e-beam evaporation as shown in Figure 3.2(g). Then, the lift-off process was performed in toluene solution under sonication for 10s, creating a hexagonal array of Al_2O_3 nanoislands of height ~ 150nm as shown in Figure 3.2(h). An SEM image of the resulting Al2O3 nanoisland structure is shown in Figure 3.2(i).

GaAs single-junction solar cells were grown by metallorganic chemical vapor deposition (MOCVD) at 100torr using Arsine (AsH_3), Phosphine (PH_3), Trimethylindium (TMI) and Trimethylgallium (TMG) as precursors with a V/III ratio > 50 on GaAs substrates. The resulting epi-layers consist of InGaP window and back surface (BSF) layers, a 3.5 μm GaAs base layer with $2\times10^{17}cm^{-3}$ p-type doping, and a 0.1 μm GaAs emitter layer with n-type doping in the range of $2\times10^{18}cm^{-3}$.

Numerical simulations were performed using the Rsoft Diffractmod software package (Rsoft Design Group, Inc., Ossining, NY, USA) and standard literature values for optical constants. [70] Incident light was assumed to be in the form of a plane wave impinging on the device surface. A simulated absorption spectrum was computed assuming optical absorption proportional to the square of the electric field amplitude, and the simulated E.Q.E. was computed assuming 100% efficiency in photo-generated carrier collection.

Optical transmittance measurements of moth-eye textured PET sheets were performed using collimated light from a halogen lamp spectrally resolved by a

monochromator based system from Optronic Laboratories with AC lock in detection. The monochromatic light was linearly polarized by a Glan-Thompson polarizer before reaching the device. Devices were mounted on a rotating stage, allowing measurements to be performed at angles of 0^o to 75^o and at wavelengths ranging from 400 nm to 1100 nm. Photocurrent response spectra were measured at zero bias using the same monochromator system. The calculated J_{sc} for devices of each type under different incident angles was derived from E.Q.E. measurements weighted by the AM1.5G solar spectrum, given by Equation 3.1:

$$J_{sc} = e\int EQE(\lambda)\,\mathrm{I}_{AM1.5}(\lambda)d\lambda \ , \qquad (3.1)$$

where e is the electron charge magnitude, and $I_{AM1.5}(\lambda)$ is the AM1.5G photon flux intensity.

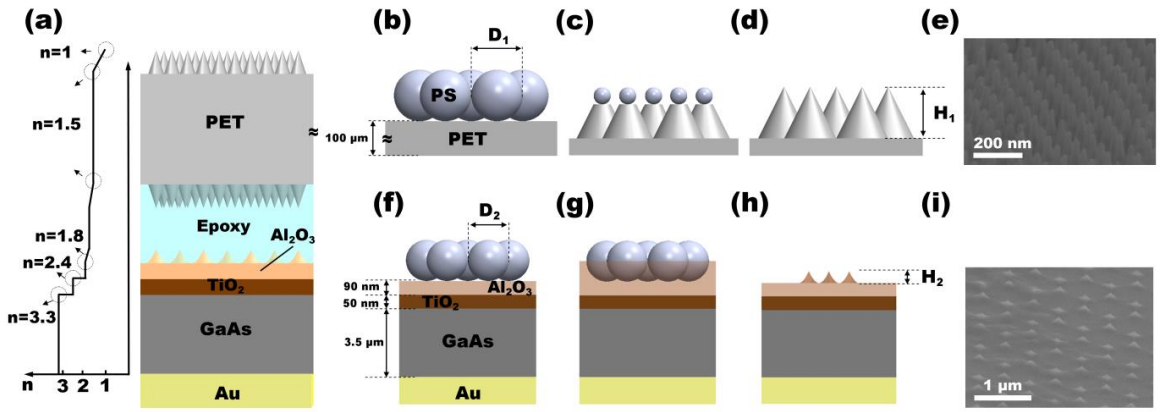

Figure 3.2. (a) Schematic diagram of a polymer-packaged single-junction GaAs solar cell coated with conventional Al_2O_3/TiO_2 bilayer thin-film antireflection coating with Al_2O_3 nanoisland structure and moth-eye textured PET packaging sheet by space-graded encapsulant, together with a schematic diagram of the refractive index profile. (b)-(d) Schematic diagrams of the process flow for fabricating moth-eye textured PET packaging sheet. (e) SEM image of fabricated moth-eye structure on PET substrate. (f)-(h) Schematic diagrams of the process flow for fabricating Al_2O_3 nanoislands. (i) SEM image of the fabricated Al_2O_3 nanoisland structure.

3.2.2 Optimization of moth-eye textured PET packaging sheets

In order to create the moth-eye textured PET packaging sheet that provides the optimum omnidirectional, broadband antireflection performance, we fabricated double-side patterned moth-eye textured PET sheet with different heights. Figure 3.3(a) shows the measured optical transmittance as a function of the incident angle for an unpatterned PET sheet and double-side moth-eye textured PET sheet with D_1 = 200nm, and different heights H_1 varying from 300nm to 600nm under TE-polarized illumination. It is observed that moth-eye nanostructures with all heights show superior transmittance characteristics compared to that of the unpatterned PET sheet at the wavelength range of 400nm to 1100nm and from incident angles from 0^o to 75^o. Similar transmittance measurements were carried out for TM-polarized light as shown in Figure 3.3(b). For TM-polarized light, the dependence of transmittance on the incident angle is much weaker compared to that of TE-polarized light due to the high transmittance that occurs near Brewster's angle. As a consequence, in this study we focus on comparing the transmittance characteristics of TE-polarized light. Figure 3.3(c) shows the transmittance measurements for unpatterned and moth-eye textured PET sheet under 0^o of incidence, and ~ 5% improvement in transmittance is observed for all moth-eye textured sheet compared to the unpatterned PET sheet. Figure 3.3(d) shows the transmittance measurements for unpatterned and moth-eye textured PET sheet at an incident angle of 75^o. It is observed that the double-side moth-eye texture PET sheet with height H_1 = 400nm shows the best transmittance performance compared to other geometries, with ~ 40% enhancement in transmittance near the wavelength of 600nm. This observation also suggests that the antireflection performance of moth-eye textured PET sheet saturates at certain height

since moth-eye textured PET sheet with even higher H_1 show improved transmittance characteristics but of less magnitude compared to the moth-eye structure with H_1 = 400nm.

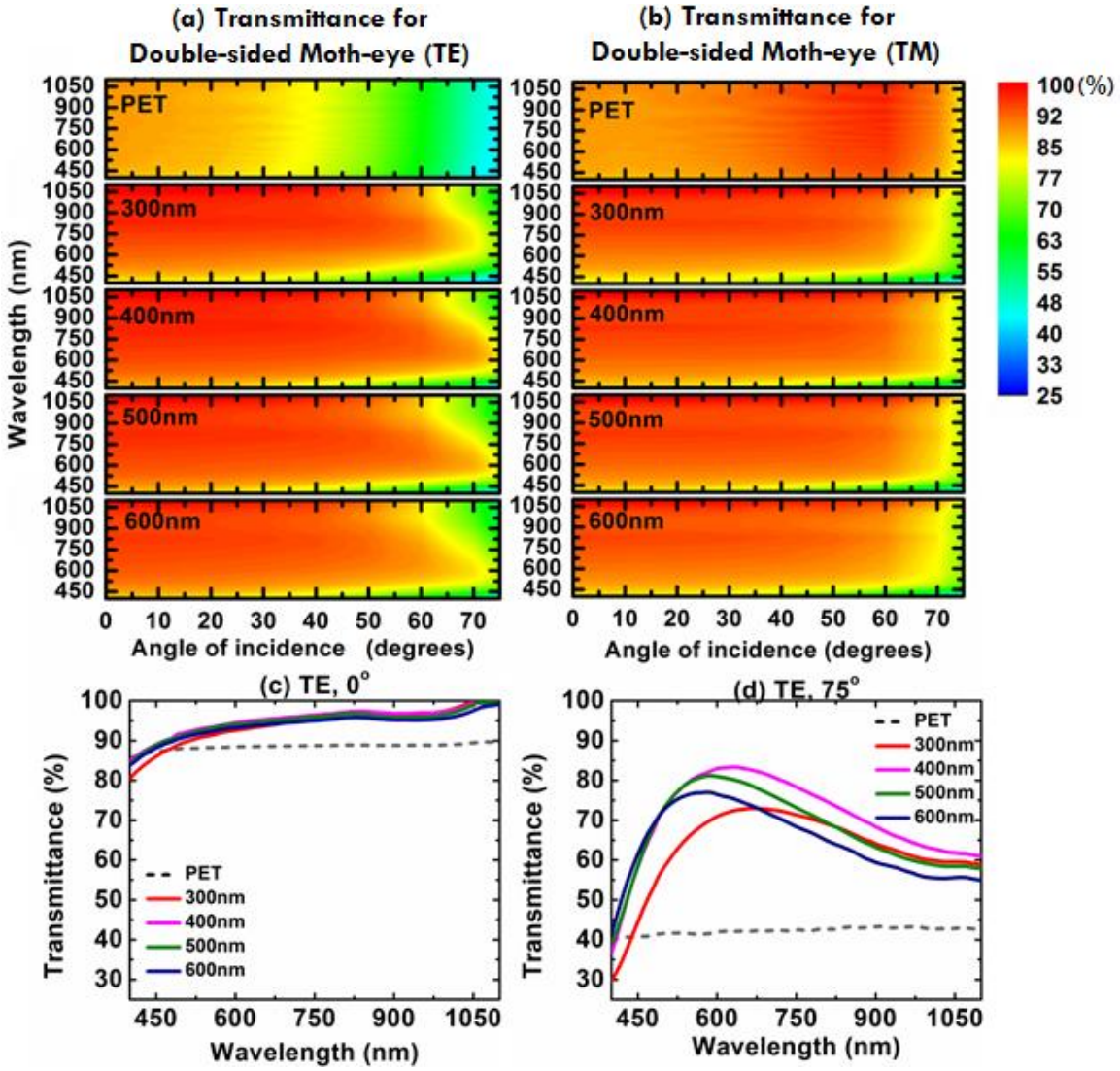

Figure 3.3. (a), (b) Transmittance measurements for the unpatterned and double-side moth-eye textured PET packaging sheet of various texturing depths with TE/TM-polarized incident light. (c), (d) Transmittance measurements for the unpatterned and double-side moth-eye textured PET packaging sheet of various texturing depths at incident angles of 0^{o} and 75^{o} under TE-polarized light illumination.

3.2.3 Optimization of dielectric nanoisland structure

The moth-eye textured PET sheet is able to provide improved antireflection performance by effectively reducing the air/PET interface Fresnel reflection via the graded refractive index profile from air to the PET substrate. In order to further reduce the interface reflection between the encapsulant and the Al_2O_3 thin-film antireflection layer, Al_2O_3 nanoisland array structures were employed. Figure 3.4(a) shows schematic diagrams of single-junction GaAs solar cells coated with conventional Al_2O_3/TiO_2 bilayer thin-film antireflection coating with and without Al_2O_3 nanoislands. Figure 3.4(b) shows the simulated GaAs cell absorption at normal incidence as a function of the incident wavelength and sphere diameter D_2 for incident angles at $\theta = 0^o$ and 80^o. The texturing height H_2 is fixed at $H_2 = D_2/2$. At normal incidence ($\theta = 0^o$), the overall absorption is close to 100% for the entire range of D_2, except for two minima observed at wavelengths between 310nm and 330nm, and between 370nm and 420nm. These absorption minima arise from Fabry-Perot resonances associated with the underlying Al_2O_3/TiO_2 bilayer thin-film antireflection coating, and they play a less significant role in determining the cell's overall photovoltaic performance since the E.Q.E. of the GaAs solar cell at these wavelengths is low, and the solar irradiance at these wavelengths is significantly lower than that at the visible wavelength range.

For the incident angle of 80^o, the Al_2O_3 nanoisland structure plays a more important role in the cell's overall photovoltaic performance. The maximum absorption is observed for $D_2 > 500$nm, due to the improved transmittance at the encapsulant/Al_2O_3 thin-film antireflection layer interface because of the graded refractive index profile of the Al_2O_3 nanoisland structure. In addition to the absorption minima observed at

wavelengths between 310nm and 330nm, and between 370nm and 420nm, additional straight interference patterns are observed for D_2 > 500nm. Similar interference patterns are observed in the simulated transmittance for the Al_2O_3 nanoisland structure on bulk Al_2O_3 (as shown in the inset) for the incident angle θ = 80°, with interference line positions very close to those observed in the absorption contour map for structure (i) at the incident angle θ = 80°. These observations reveal that the physical origin of the interference pattern observed in the GaAs cell absorption contour map at the incident angle θ = 80° results from the Fabry-Perot interferences inside the Al_2O_3 nanoisland structure for certain combinations of wavelength and structural parameters. Hence, we conclude that for the optimized antireflection performance, the diameter/height of the Al_2O_3 nanoisland structure can be chosen in the range 500nm < D_2 <1000nm, since even taller structures can only provide a limited degree of improvement, and those structures are impractical to fabricate. Figure 3.4(c) shows the measured E.Q.E. spectra for structure (i) with D_2 = 1000nm (solid lines), and structure (ii) (dashed lines) under different incident angles. For smaller incident angles (θ < 80°), both structures show similar E.Q.E. spectra; while at larger incident angles (θ = 80°), the GaAs cell integrated with additional Al_2O_3 nanoisland structures shows improved antireflection performance over the entire wavelength range.

3.2.4 Integrated optical nanostructures on bulk GaAs solar cells

Figure 3.5(a) shows schematic diagrams of single-junction GaAs solar cells with various antireflection configurations under comparison in this study, including (i) GaAs solar cell without Al_2O_3 nanoislands integrated with unpatterned PET packaging sheet; (ii)

GaAs solar cell with Al_2O_3 nanoislands integrated with unpatterned PET packaging sheet; (iii) GaAs solar cell without Al_2O_3 nanoislands integrated with double-side moth-eye patterned PET packaging sheet; and (iv) GaAs solar cell with Al_2O_3 nanoislands integrated with double-side moth-eye patterned PET packaging sheet. Figure 3.5(b) shows the measured E.Q.E. spectra for all four device types. Clearly, structures (ii), (iii) and (iv) show substantially improved E.Q.E. compared to the unpatterned cell (i), particularly at incident angles $\theta > 70^o$. J_{sc} calculated for cells with each configuration, derived from E.Q.E. measurements under different incident angles, is shown in Figure 3.5(c). First, it is observed that structure (ii) shows similar J_{sc} compared to the reference structure (i) at small incident angles, and improved antireflection performance at large incident angles due to the graded refractive index profile at the encapsulant/Al_2O_3 interface. This observation is consistent with our simulation results shown in Figure 3.4. Second, we observe that structure (iii) shows substantial improvement in J_{sc} over the entire range of incident angles compared to structrues (i) and (ii), which is due to the graded transition in refractive index from air to the PET packaging sheet substrate. Finally, it is observed that structure (iv), the GaAs solar cell with Al_2O_3 nanoisland structure and integrated with moth-eye textured PET packaging sheet, shows further improved J_{sc} compared to other structures over the entire range of incident angles. These measurement and calculation results demonstrate that our integrated optical nanostructures effectively reduce Fresnel reflection at each key interface in the fully packaged structure. Figure 3.5(d) shows the calculated ratio of J_{sc} of structure (iv) over that of structures (i), (ii) and (iii) with incident angles varying from 0^o to 80^o. We observe that ~ 10% increase in J_{sc} at normal incidence, and ~ 67% increase in J_{sc} at 80^o incidence

is achieved for structure (iv) compared to the reference cell of structure (i). This observation suggests that our approach can be very promising in improving the solar cell efficiency for wide ranges of incident angles in various photovoltaic applications.

3.2.5 Conclusion

We have demonstrated and analyzed the broadband, omnidirectional antireflection performance of single-junction GaAs solar cells combined with Al_2O_3 nanoisland array structures and moth-eye textured PET packaging sheet, which shows substantial improvement in the calculated J_{sc} derived from E.Q.E. measurements under various incident angles compared to the reference cell without antireflective optical nanostructures. Transmittance measurements were carried out for moth-eye textured PET sheet with 200nm period and with various texturing depths. It is observed that structures with texturing depth of 400nm provide the optimum antireflection performance, maintaining > 90% transmittance at the wavelength range of 400nm to 1050nm at normal incidence, and maintaining > 70% transmittance at the wavelength range of 500nm to 900nm at 80^o incidence. The choice of the dimension of the Al_2O_3 nanoisland structure is guided by detailed numerical simulation. Finally, calculated J_{sc} derived from E.Q.E. measurements shows that the single-junction GaAs solar cell with Al_2O_3 nanoislands integrated with a moth-eye textured PET packaging sheet yields ~ 10% increase in J_{sc} compared to the reference cell without antireflective optical nanostructures at normal incidence, and ~ 67% increase at 80^o incidence. This observation suggests that our approach is a highly promising antireflection strategy, scalable via low-cost manufacturing techniques, for various photovoltaic applications, especially for those in

concentrated photovoltaic systems or mobile solar systems where solar energy harvesting over wide ranges of incident angles and wavelengths are particularly desirable.

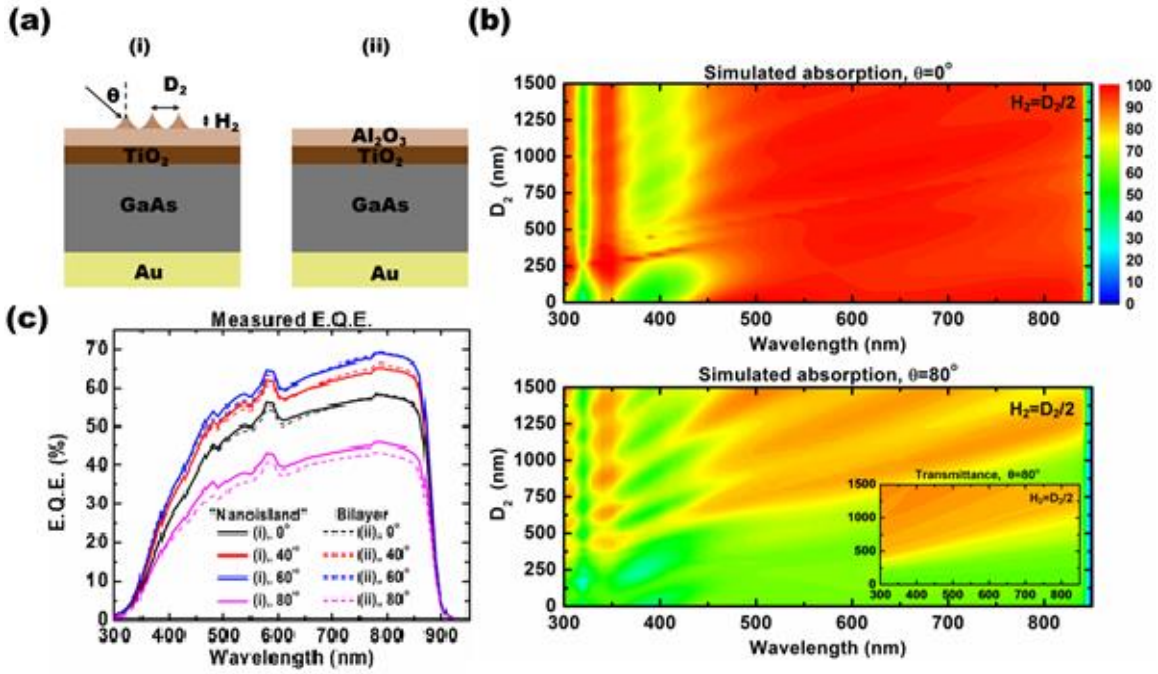

Figure 3.4. (a) Schematic diagrams of single-junction GaAs solar cells coated with conventional Al_2O_3/TiO_2 bilayer thin-film antireflection coating with and without Al_2O_3 nanoislands. (b) (Top) Simulated GaAs cell absorption at normal incidence for incident wavelengths from 300nm to 850nm with the sphere diameter D_2 varying from 0nm to 1500nm while fixing the nanoisland height $H_2 = D_2/2$. (Bottom) Simulated cell absorption for same structural parameters and the same wavelength range at 80^o incidence. The incident light was polarized at 45^o to include the same amount of TE and TM polarizations simultaneously. (c) Measured E.Q.E. spectra for single-junction GaAs cells with and without Al_2O_3 nanoislands.

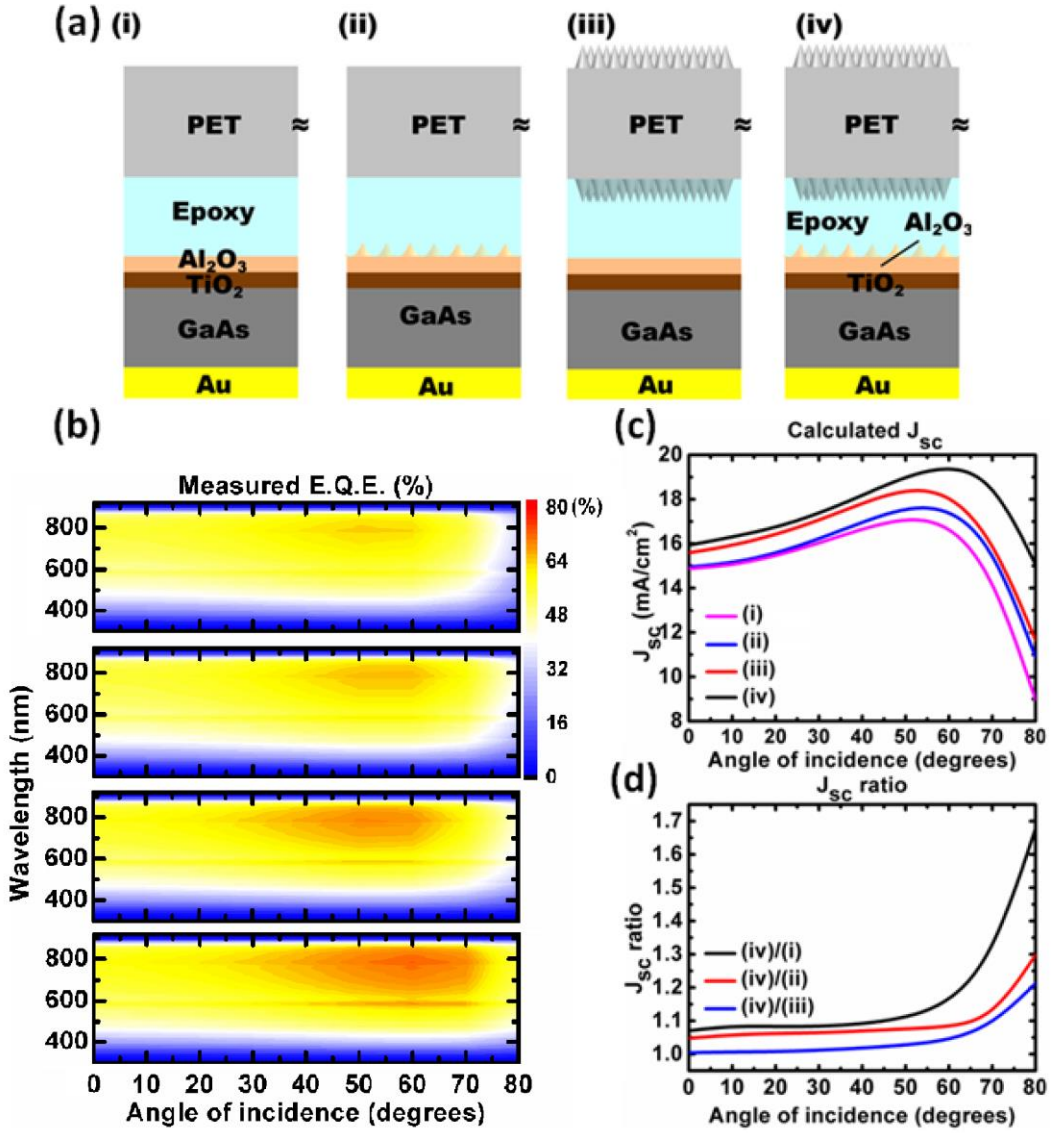

Figure 3.5. (a) Schematic diagrams of various integrated structures under comparison: (i) GaAs solar cell without Al_2O_3 integrated with conventional Al_2O_3/TiO_2 bilayer thin-film antireflection coating. (ii) GaAs solar cell with Al_2O_3 nanoislands integrated with unpatterned PET packaging sheet. (iii) GaAs solar cell without Al_2O_3 nanoislands integrated with moth-eye textured PET packaging sheet. (iv) GaAs solar cell with Al_2O_3 nanoislands integrated with moth-eye textured PET packaging sheet. (b) Measured E.Q.E. spectra for devices of all types. (c) Calculated J_{sc} for devices of each type, derived from E.Q.E. measurements weighted by AM1.5G solar spectrum. (d) Calculated J_{sc} ratio of structure (iv) over that of structures (i), (ii) and (iii) with the incident angle varying from 0^o to 80^o.

3.3 INTEGRATED OPTICAL NANOSTRUCTURES ON FLEXIBLE, EPITAXIAL LIFT-OFF (ELO) GAAS SOLAR CELLS FOR BROAD-SPECTRUM, OMNIDIRECTIONAL PHOTOVOLTAIC PERFORMANCE IMPROVEMENT

In section 3.3, we further extend this approach to flexible, epitaxial lift-off (ELO) GaAs solar cells. We show that our integrated optical nanostructures provide a comparably good antireflection performance on flexible, ELO GaAs solar cells as that on bulk GaAs solar cells: compared to the unpatterned cell, a $1.09\times$ increase in J_{sc} is observed for the cell integrated with optical nanostructures at normal incidence, while a $1.52\times$ increase in J_{sc} is observed at 80^{o} angle of incidence. Photovoltaic performance of our integrated optical nanostructures on flexible, ELO GaAs solar cells under different bending radii has been studied: the unpatterned cell yields a 9.7% decrease in J_{sc} under a moderate bending condition whilst the cell integrated with optical nanostructures yields a 6.7% decrease in J_{sc} under the same bending condition. Additionally, the superior self-cleaning properties of the moth-eye textured PET packaging sheet have been demonstrated.

3.3.1 Epitaxial lift-off GaAs solar cells

Over the last several years, the efficiency of III/V solar cells has increased significantly, [57, 58] and so has the demand for high efficiency III/V solar cells in various photovoltaic applications, such as in concentrated and mobile PV systems. However, one of the major factors limiting the large-scale deployment of III/V high efficiency solar cells is their cost. [59-61] The epitaxial lift-off technique, [62-65] which enables the separation of epitaxially-grown thin-film device layer from the substrates and reuse of the original growth substrates, effectively reduces the production cost for high

efficiency III/V solar cells and paves the way for integration of high efficiency III/V solar cells at large scale.

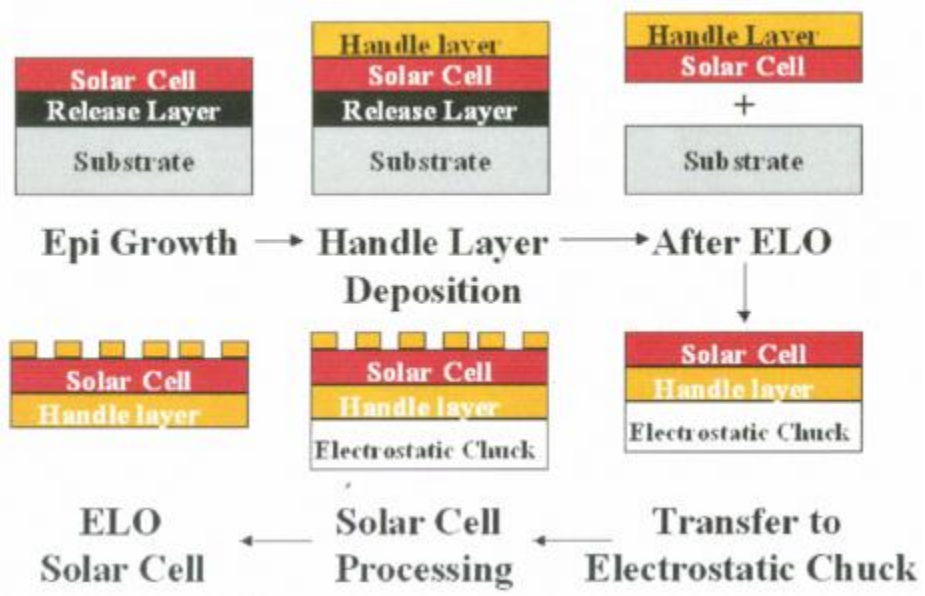

Figure 3.6 Schematic diagram of the process flow for fabricating thin-film epitaxial lift-off (ELO) cells. [66]

Figure 3.6 shows the typical process flow for creating thin-film, flexible GaAs solar cells via epitaxial lift-off. The single-junction GaAs solar cell device layer is grown on GaAs substrates in reverse order, preceded by a thin AlGaAs release layer. Followed by a selective wet etching process, the thin-film device layer is then separated from the original growth substrate, and transferred to the handle layer for subsequent patterning processes.

Other important advantages for ELO cells are the substantially reduced cell weight, and the superior flexibility that make them particularly suitable for space and portable photovoltaic applications. [67, 68] As a consequence, it is of essential importance to develop and integrate a broad-spectrum, omnidirectional antireflection

coating on flexible, ELO solar cells so that the cell efficiency can be improved over broad ranges of incident angles and wavelengths.

3.3.2 Experiment

GaAs single-junction solar cells for the epitaxial lift-off process were grown by MOCVD in the similar way as described in section 3.3.1, except that an additional 5nm AlAs release layer was grown between the epitaxial device layer and the GaAs substrate. The epitaxial lift-off process was performed via a procedure reported elsewhere. [69]

Current-voltage characteristics were measured using a Newport Oriel 96000 solar simulator operating at 1-sun illumination with an airmass (AM) 1.5G filter. Photocurrent response spectra were measured at zero bias using a single-grating monochromator based system from Optronic Laboratories with AC lock in detection, under unpolarized light. The PET packaging sheet is used to attach to the cell substrate using a space-grade encapsulant. A home-made stretcher is used to bend the packaged ELO cells.

Figure 3.7(a) shows the schematic diagram of an ELO single-junction GaAs solar cell with conventional Al_2O_3/TiO_3 thin-film bilayer antireflection coating integrated with Al_2O_3 nanoisland structure and double-side moth-eye textured PET packaging sheet, together with the refractive index profile. Figure 3.7**(**b)-(d) show key steps in fabricating the moth-eye textured PET packaging sheet: D_1 = 200nm diameter PS spheres were deposited on the PET packaging sheet surface using the NSL process (Figure 3.7**(**b)), followed by reactive-ion etching with 100sccm of oxygen at a pressure of 200mTorr and radio frequency power of 100W for 4min (Figure 3.7**(**c)), resulting in the moth-eye textured surface (Figure 3.7**(**d)) with a nanostructure height H_1 = 400nm. Figure 3.7**(**e)-(g)

show key steps in fabricating the Al_2O_3 nanoisland structure on ELO GaAs cell surface: D_2 = 1000nm PS spheres were deposited on the cell surface using the NSL process (Figure 3.7(e)), followed by e-beam evaporation of 500nm Al_2O_3 (Figure 3.7**(**f)); a lift-off process in toluene performed under sonication for 5s completed the fabrication process for the Al_2O_3 nanoislands (Figure 3.7**(**g)), with nanoisland height H_2 ~ 150nm. Scanning electron microscope (SEM) images of the fabricated moth-eye textured PET sheet surface and Al_2O_3 nanoisland array are shown in Figure 3.7**(**h) and **(**i), respectively. With the gradual change in the refractive index at each key interface created by the double-side textured PET packaging sheet and Al_2O_3 nanoislands, the photovoltaic performance of the ELO GaAs cell is substantially improved over wide ranges of incident angles and wavelengths.

3.3.3 Integrated optical nanostructures on flexible, ELO GaAs solar cells

Figure 3.8(a) shows schematic diagrams of the three structures we are comparing in this study: (i) ELO single-junction GaAs solar cell with conventional Al_2O_3/TiO_2 bilayer antireflection coating integrated with unpatterned PET packaging sheet; (ii) ELO single-junction GaAs solar cell with conventional Al_2O_3/TiO_2 bilayer antireflection coating integrated with double-side moth-eye textured PET packaging sheet; and (iii) ELO single-junction GaAs solar cell with conventional Al_2O_3/TiO_2 bilayer antireflection coating integrated with Al_2O_3 nanoisland structure and double-side moth-eye textured PET packaging sheet. A photograph of the completely integrated ELO GaAs solar cell is shown in Figure 3.8(b). Figure 3.8(c) show the measured current-voltage characteristics for the each device under different incident angles, in which J_{sc} is calculated as the

measured current value divided by the total cell area ~1.1cm^2. Compared to structure (i), structure (ii) shows substantially improved J_{sc} value over the entire range of incident angles thanks to the reduced Fresnel reflection at the air/PET interface via the moth-eye textured structure. Compared to structures (i) and (ii), structure (iii) shows further improved J_{sc} value over the entire range of incident angles, which demonstrates the effectiveness of these integrated optical nanostructures in improving cell's light energy harvesting efficiency over a broad range of incident angles. Figure 3.8(d) shows the calculated J_{sc} ratio of the completely integrated structure (iii) over that of structures (i) and (ii). A $1.09\times$ increase in J_{sc} is observed for the completed integrated structure (iii) compared to the structure (i) without optical nanostructures at normal incidence, and a $1.52\times$ increase in J_{sc} is observed at 80^o angle of incidence.

Figure 3.9(a)-(d) show the measured E.Q.E. for structures (i)-(iii) at incident angles of 0^o, 60^o, 70^o, and 80^o, in which the change in total illumination incident on the cell area at each incident angle is taken into account, so that E.Q.E. is calculated assuming that the incident light intensity does not change with the varying incident angle. For the creation of Al_2O_3 nanoisland structure studied in this set of measurements, we performed the fabrication process similar to that described in section 3.3.2, but instead of using PS spheres of 1000nm in diameter; we used PS spheres of 750nm in diameter, and subsequent e-beam evaporation of 375nm of Al_2O_3 instead of 500nm. Based on the numerical calculation reported elsewhere, [71] the optimal photovoltaic performance for the Al_2O_3 nanoisland structure is achieved for PS spheres of diameters greater than 500nm, and the photovoltaic performance of the Al_2O_3 nanoisland structure differs very little with PS spheres of diameters greater than 500nm.

Compared to the structure (i) which is without optical nanostructures, structure (ii) yields overall improved photovoltaic performance over the entire range of incident angles thanks to the reduced Fresnel reflection at the air/PET interface via the moth-eye textured structure. Note that at the incident angle of 80^o, structure (ii) yields slightly decreased E.Q.E. compared to that of structure (i) at wavelengths > 740nm, which we attribute to fabrication imperfections. Structure (iii) yields very similar photovoltaic performance at incident angles of 0^o, 60^o, and 70^o, and further improved photovoltaic performance at 80^o angle of incidence compared to structure (ii). This observation demonstrates the effectiveness of this approach in boosting the photovoltaic performance of flexible, ELO solar cells over a broad range of incident angles.

Figure 3.10(a) shows the measured current-voltage characteristics for structures (i) and (iii) under AM1.5G, 1-sun illumination, under both flat and bent conditions. Figure 3.10(b) shows that the flexible, ELO cells were bent using a home-made stretching apparatus, to a radius of curvature of ~3cm. It is observed that structure (i) yields a J_{sc} ~ 16.20mA/cm^2 at flat condition, and J_{sc} ~ 14.63mA/cm^2 at bent condition, corresponding to a 9.7% reduction in J_{sc} from flat to bent condition. On the other hand, structure (iii) yields a J_{sc} ~ 18.14mA/cm^2 at flat condition, and J_{sc} ~ 16.92mA/cm^2, corresponding to a 6.7% reduction in J_{sc} from flat to bent condition significantly smaller than that observed for structure (i). We attribute the improved J_{sc} of structure (iii) to the substantially improved transmission for TE polarized component of the incident light, [71] and the slightly decreased V_{oc} values for both structures to the reduction in photocurrent density under bent condition.

3.3.4 Self-cleaning properties of moth-eye textured PET packaging sheet

In real photovoltaic applications, cell efficiency tends to degrade with the accumulation of dust and contaminants in air on the cell surface, [72-75] which reduces cell's optical absorption efficiency. Therefore, various approaches have been studied and reported to overcome this problem, including exploiting the hydrophobic properties of biomimetic surfaces. [76-78] It is observed that the moth-eye textured PET packaging sheet in this study yields surface hydrophobic properties comparable to those reported previously. [79, 80] Figure 3.11(a) and (b) show photographs of water droplets on a piece of moth-eye textured PET packaging sheet and a piece of unpatterned PET packaging sheet, respectively. The water droplet on the moth-eye textured PET packaging sheet has a contact angle of ~ 130^{o}, significantly larger than that of the unpatterned planar PET packaging sheet which is ~ 64^{o}. This observation suggests that self-cleaning behavior is another desirable attribute of the moth-eye textured PET packaging sheet in addition to the superior omnidirectional, broad-spectrum antireflection performance.

3.3.5 Conclusion

In conclusion, we have demonstrated a practical and effective antireflection strategy that can be readily implemented on flexible, ELO solar cells, which is able to provide superior broad-spectrum, omnidirectional antireflection performance. Flexible, ELO single-junction GaAs solar cells integrated with Al_2O_3 nanoisland structure and double-side moth-eye textured PET packaging sheet is observed to yield ~ 9% increase in J_{sc} at normal incidence compared to the cell without optical nanostructures, and ~ 52% increase in J_{sc} at 80^{o} angle of incidence. Current-voltage measurements for the completed

optical nanostructures – integrated ELO cell and the ELO cell without optical nanostructures are performed at both flat and bent conditions. The ELO cell completely integrated with optical nanostructures yields a J_{sc} of ~ 18.14mA/cm^2 at flat condition, and a reduction in J_{sc} of ~ 6.7% at bent condition; while the ELO cell without optical nanostructures yields a J_{sc} of ~ 16.20mA/cm^2 at flat condition, and a reduction in J_{sc} of ~ 9.7% at bent condition. Additionally, self-cleaning properties of the moth-eye textured PET packaging sheet have been investigated and demonstrated. We anticipate that with more advanced fabrication techniques, such as roll-to-roll nanoimprint lithography, [81-84] such approach can be employed for cells with much larger areas that can be implemented in various photovoltaic applications.

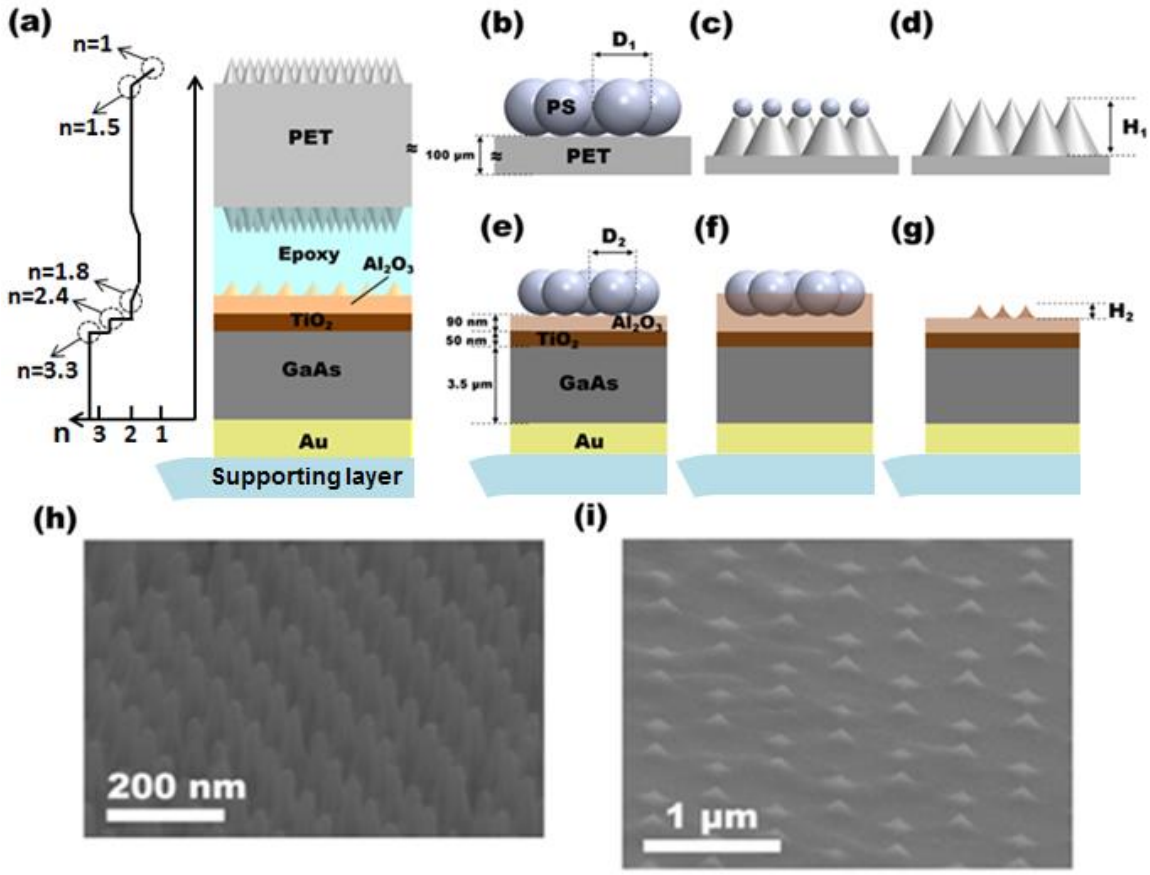

Figure 3.7. (a) Schematic diagram of a polymer-packaged GaAs solar cell coated with conventional Al_2O_3/TiO_2 bilayer antireflection coating with Al_2O_3 nanoislands and integrated with double-side moth-eye textured PET packaging sheet by space-grade encapsulant, together with the refractive index profile. (b)-(d) Schematic diagrams of process flow for fabricating moth-eye structure on PET substrate using nanosphere lithography with polystyrene spheres (PS). (e)-(g) Schematic diagram of process flow for fabricating Al_2O_3 nanoisland structure on Al_2O_3/TiO_2 bilayer antireflection coating. (h) SEM image of the completed moth-eye structure on PET substrate. (i) SEM image of the completed nanoisland structure.

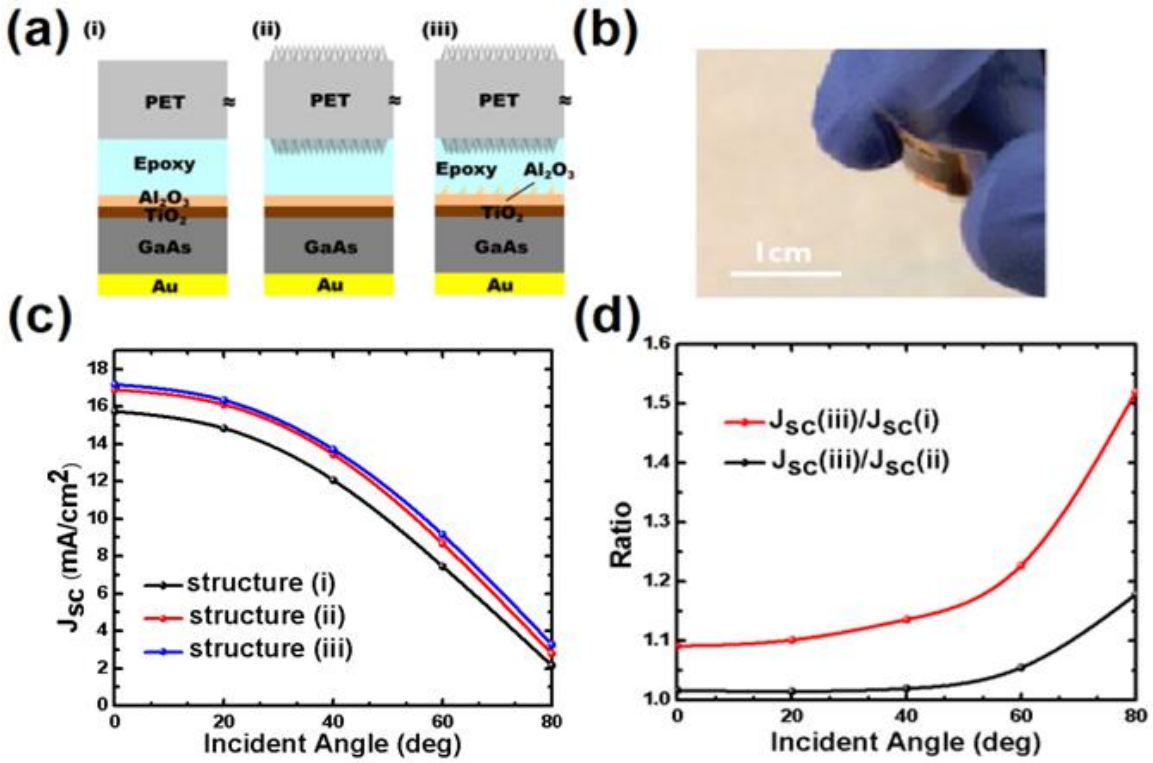

Figure 3.8. (a) Schematic diagrams of various integrated structures under comparison. (b) Photograph of ELO GaAs solar cell integrated with flexible PET packaging sheet. (c) Measured J_{sc} for each integrated structure with incident angles varying from 0^o to 80^o. (d) Calculated ratio for J_{sc} of integrated structure (iii) over that of structures (i) and (ii).

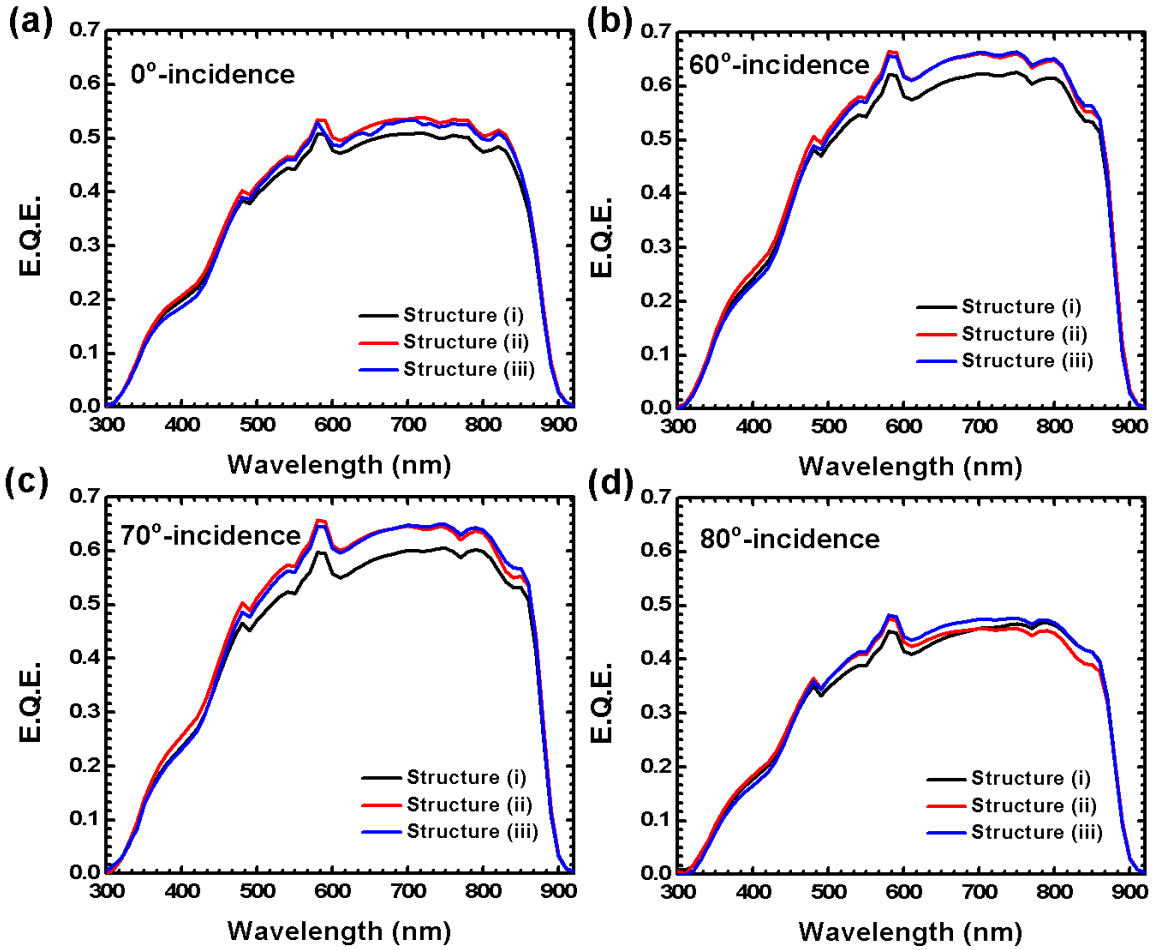

Figure 3.9. E.Q.E. measurements for structures (i)-(iii) at (a) 0^{o} angle of incidence; (b) 60^{o} angle of incidence; (c) 70^{o} angle of incidence; and (d) 80^{o} angle of incidence.

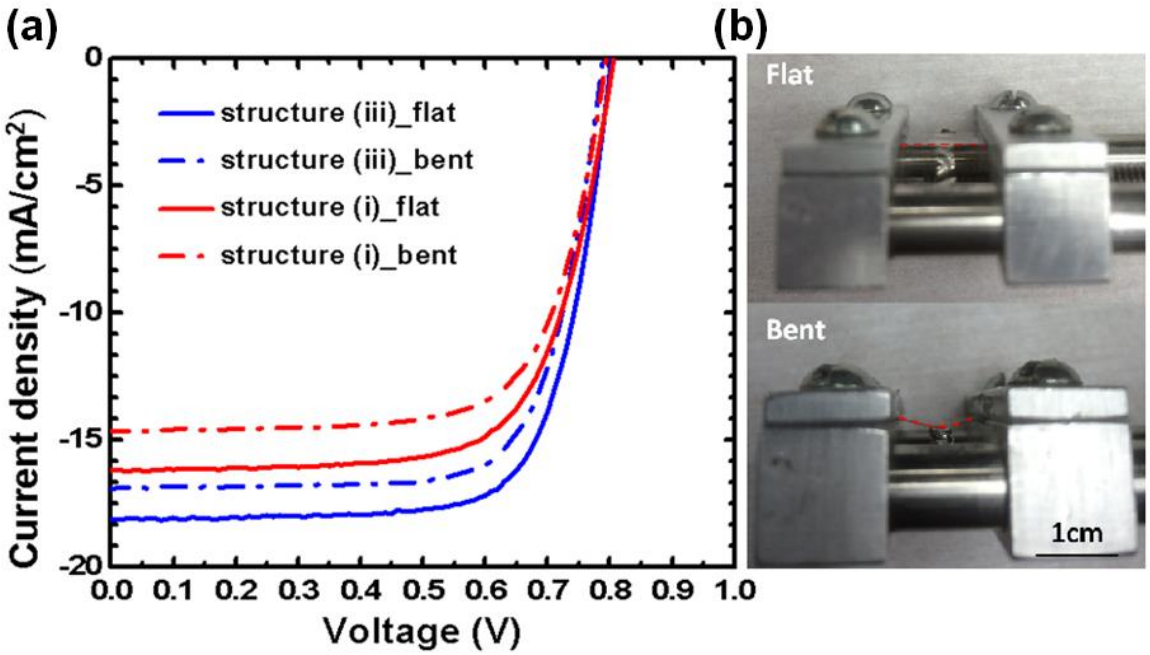

Figure 3.10. (a) Current-voltage characteristics for structures (i) and (iii) measured under flat and bent conditions under AM1.5G, 1-sun illumination. (b) Photographs of flexible ELO cells under flat and bent conditions.

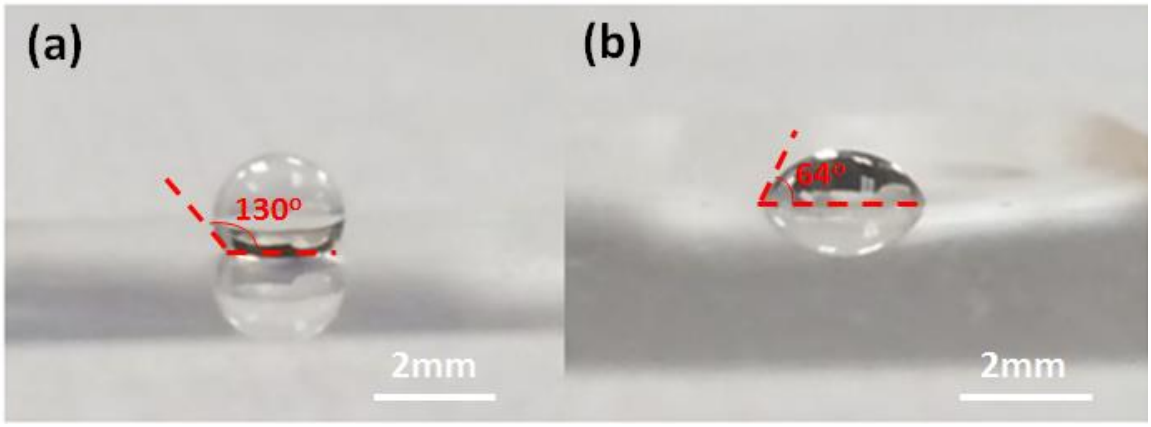

Figure 3.11. Photographs of a water droplet on (a) moth-eye textured PET packaging sheet, and (b) planar PET packaging sheet, along with the contact angles measured for each.

Chapter 4: High Efficiency GaAs/InGaAs Quantum Well Solar Cells with Bandgap Engineering Techniques

4.1 MOTIVATION

Taking the trade-off in V_{oc} and J_{sc} of a solar cell into account, studies show that in order to achieve the optimum cell efficiency, an ideal *pn* junction needs to have the bandgap to fall approximately between 1.3eV and 1.6eV. [85-87] The bandgap for GaAs falls squarely in this region, and energy conversion efficiency as high as 28.8% for single-junction GaAs solar cells has been reported recently. [88] The efficiency for *pn* junction solar cells can potentially be further improved by insertion of low-dimensional nanostructures, such as QWs, into the intrinsic region of the GaAs *p-i-n* solar cell structure, which extends the cell absorption into the sub-GaAs bandgap region. [28-32] As a consequence, QW solar cells are able to achieve higher J_{sc} compared to conventional *pn* GaAs solar cells. However, a decreased V_{oc} is generally observed for QW solar cells as material defects can be introduced due to lattice mismatch, [89, 90] and carrier extraction efficiency can be lowered since QWs act as recombination centers for photo-generated carriers. [35-37, 91-93] In order to mitigate the reduction in V_{oc} for QW solar cells, different band-edge profiles have been studied in previous reports, including using strain-balance techniques to minimize lattice relaxation during growth, [94, 95] and designing different band-edge energy profiles, such as stepped potential barriers in QW solar cells, to improve the photo-generated carrier extraction efficiency. [40] Figure 4.1(a) shows a typical QW solar cell epi-layer structure, and Figure 4.1(b) shows the associated band-edge energy profile together with the main carrier photo-carrier generation and recombination paths in the QW region.

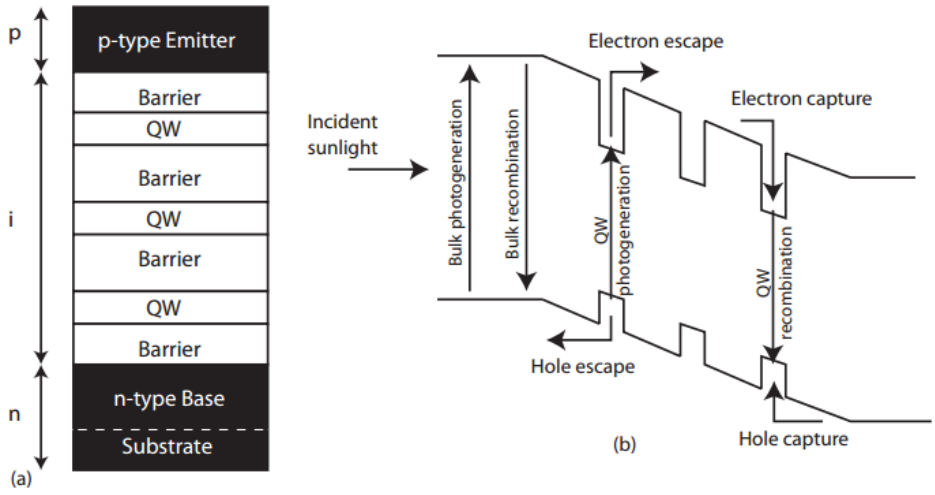

Figure 4.1. (a) A typical QW *p-i-n* layer structure; (b) Band-diagram for a typical QW p-i-n solar cell showing the photogeneration and recombination processes, together with the carrier capture and escape routes. [96]

4.2 GAAS/INGAAS QUANTUM WELL SOLAR CELLS WITH BANDGAP-ENGINEERED GRADED QUANTUM WELL DEPTHS

In this section, we demonstrate and analyze a bandgap engineering technique for thin-film *p-i-n* GaAs/InGaAs QW solar cells in which indium concentration in the QW region monotonically changes from 10% to 30% which achieves a much less reduced V_{oc} while maintaining sufficiently high optical absorption in the sub-GaAs bandgap region. We demonstrate that for the GaAs/InGaAs QW solar cell with graded QW depths in the intrinsic region, photo-generated carrier concentration in the QW region can be effectively reduced at large forward bias, and both V_{oc} and J_{sc} are increased compared to the QW cell with the same indium concentration but constant QW composition across the intrinsic region by engineering the band-edge energy profile of the QW region. For QW solar cells in this study, sub-GaAs bandgap wavelength absorption has been further improved by exploiting light trapping techniques, in which backscattering structures were fabricated via a nanosphere lithography process (NSL).

4.2.1 Experiment

Epi-layer structures were grown by solid-source molecular beam epitaxy (MBE) on GaAs (001) undoped substrates shown schematically in Figure 4.2. A 200nm n-type GaAs buffer layer was grown for each sample, followed by an 800nm n-type ($n \sim 2\times10^{18}$cm^{-3}) $Al_{0.85}Ga_{0.15}As$ etch stop layer, 20nm n-type ($n \sim 6.5\times10^{18}$cm^{-3}) GaAs contact layer, and 30nm n-type ($n \sim 3\times10^{18}$cm^{-3}) $Al_{0.85}Ga_{0.15}As$ window layer. A 100nm n-type ($n \sim 3\times10^{18}$cm^{-3}) GaAs emitter layer was grown next, followed by an unintentionally doped layer consisting of either 134nm GaAs (structure (i)) or GaAs/InGaAs QW structures (structures (ii)-(v)) with a total intrinsic region thickness of 134nm. A 2000nm p-type (Be-doped, $p \sim 5\times10^{17}$cm^{-3}) GaAs base layer, a 100nm p-type ($p \sim 1\times10^{18}$cm^{-3}) $Al_{0.2}Ga_{0.8}As$ back surface field layer and a 20nm thick p-type ($p \sim 5\times10^{18}$cm^{-3}) GaAs contact layer then completed each epitaxial layer structure. The growth temperature was kept above 500^{o}C throughout. For intrinsic GaAs, the background doping concentration from impurities in the chamber is below the threshold of Hall measurements, and is therefore estimated to be below 10^{15}cm^{-3}. Band-edge energy diagrams of QW cell structures in this study were calculated using a 1D Poisson solver, [97] with constant separation of electron and hole quasi-fermi levels (QFL) throughout the intrinsic region assumed.

Current-voltage characteristics were measured using normally incident light from a Newport Oriel 96000 solar simulator operating at 1-sun illumination with an airmass (AM) 1.5G filter. Photocurrent response spectra were measured at zero bias using a single grating monochromator based system from Optronic Laboratories with AC lock in detection.

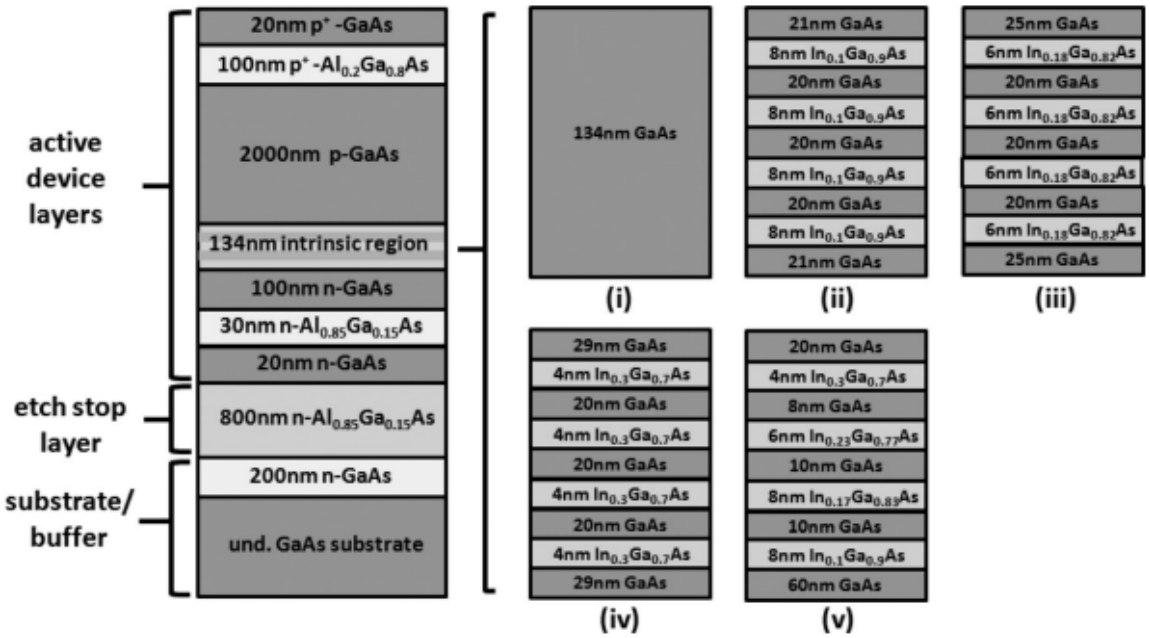

Figure 4.2. Schematic diagram of epitaxial layer structures for (i) GaAs homojunction cell structure; (ii) GaAs/$In_{0.1}Ga_{0.9}As$ QW cell structure; (iii) GaAs/$In_{0.18}Ga_{0.82}As$ QW cell structure; (iv) GaAs/$In_{0.3}Ga_{0.7}As$ QW cell structure; (v) graded QW cell structure. Active device layers, etch stop layers, and substrate/buffer layers labeled for each correspond to similarly labeled sample layers in Figure 4.3.

Key steps in the device fabrication process flow are illustrated in Figure 4.3(a)-(d). A 100nm SiO_2 layer was e-beam evaporated onto the epi-grown p^+-GaAs surface, followed by patterning using the NSL process, in which 500nm diameter polystyrene spheres were deposited on the SiO_2 surface in a hexagonal array using a Langmuir-Blodgett process (Figure 4.3(a)). [47] Reactive-ion-etching was used to shrink the sphere diameter from 500nm to 250nm, followed by deposition of 15nm Cr, a lift-off process in toluene under sonication, and then reactive-ion-etching of the SiO_2 layer with a CF_4/O_2 gas mixture (Figure 4.3(b)). 10nm Cr/40nm Au/1200nm In metallization was then deposited to form the nanostructured rear contact (Figure 4.3(c)). Then, using a home-built wafer-bonding apparatus, the cell structure was flip-bonded to a silicon substrate on which 10nm Cr/800nm Au had previously been deposited by e-beam evaporation. Finally,

substrate removal and mesa etching processes were employed to create 1mm × 1mm and 2mm × 2mm device mesas on the silicon supporting substrates, and the devices were coated with a 76nm silicon nitride antireflection coating (Figure 4.3(d)). Additional details regarding the thin-film device fabrication process have been reported elsewhere. [17, 53, 98]

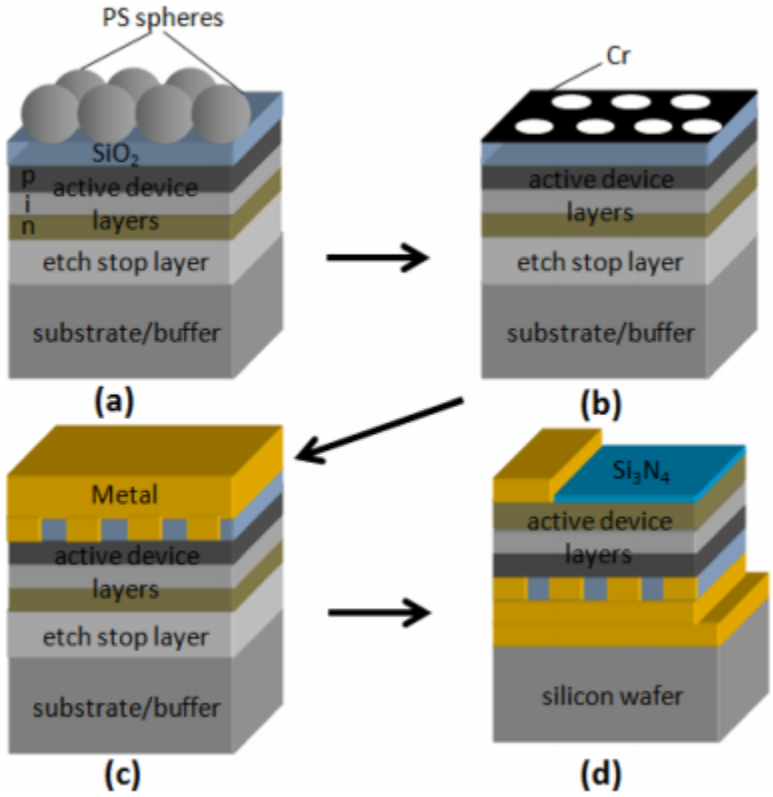

Figure 4.3. Key steps in process flow for fabrication of complete thin-film solar cell devices integrated with nanostructured metal/dielectric rear contacts bonded onto silicon substrates. (a) 100nm SiO_2 layer was e-beam evaporated onto the cell surface, followed by a NSL process, in which a hexagonal array of 500nm diameter polystyrene spheres was created on the SiO_2 surface. (b) A Cr hard mask was created after polystyrene sphere diameter shrinking using reactive-ion-etching, followed by e-beam evaporation of 15nm Cr, and a lift-off process in which polystyrene spheres were dissolved in toluene under sonication. (c) The nanostructured rear contact was formed by e-beam deposition of 10nm Cr/40nm Au/1200nm In metallization. (d) The cell structure was flip-bonded to a silicon substrate on which 10nm Cr 800nm Au metallization had previously been e-beam deposited, and 1mm × 1mm and 2mm × 2mm device mesas were created after a substrate removal and mesa etching process, and coated with a 76nm silicon nitride antireflection coating.

4.2.2 Simulation and measurement results

The key idea for the graded GaAs/InGaAs QW solar cell structure design is that it enables increased separation of the electron QFL from the QW conduction band-edge at large forward bias, resulting in a substantially reduced photo-generated carrier density inside QWs at forward bias, and consequently increased V_{oc} and the operating voltage for maximum power output. At the same time, for the graded QW cell structure, the QW barriers can be much thinner compared to those in reference QW cells while remaining below the critical thickness for strain relaxation so that photo-generated carrier tunneling is facilitated.

Figure 4.4(a) shows the band-edge energy profile for the GaAs/$In_{0.1}Ga_{0.9}As$ QW cell under a forward bias of 0.8V computed using a 1D Poisson solver. It is expected that if there exists a significant overlap of the electron QFL with the QW conduction band-edge, the photo-generated carrier collection efficiency will be greatly reduced due to the high concentration of photo-generated carriers inside the QWs, and a V_{oc} as high as 0.8V cannot be maintained. For the GaAs/$In_{0.1}Ga_{0.9}As$ QW cell, which has the set of QWs with shallowest QW depths, a small overlap of the electron QFL with the InGaAs QW conduction band-edge is observed. However, it is relatively a minor factor in determining the cell's V_{oc} due to the lower electronic density of states in the conduction band of GaAs/$In_{0.1}Ga_{0.9}As$ QWs compared to QWs in other cells under this study with higher In concentration. Figure 4.4(b) and (c) show the computed band-edge energy profile for GaAs/$In_{0.18}Ga_{0.82}As$ and GaAs/$In_{0.3}Ga_{0.7}As$ QW cells under a forward bias of 0.8V via 1D Poisson solver. A large overlap of the electron QFL with the QW conduction band-edge is observed for both structures, indicating that at a forward bias of 0.8V, a

significant concentration of photo-generated carriers is trapped inside QWs instead of being extracted, which will result in a degraded V_{oc}. Figure 4.4(d) shows the computed band-edge energy profile for the QW cell structure with graded QW depths at a forward bias of 0.8V via 1D Poisson solver. The electron QFL is clearly well below the QW conduction band-edge, which ensures that a low photo-generated carrier concentration is trapped inside the QWs instead of being extracted at this forward bias. Note that with regard to carrier concentrations inside QWs, the assumption that the electron QFL stays constant across the intrinsic region is essentially the most conservative assumption, and the actual carrier concentration in the QWs can be lower. [99-101] On the other hand, the graded QW design enables the electron QFL to stay well below the QW conduction band-edge, resulting in reduced QW carrier concentration at large forward bias voltages. In this study, the average indium concentration for the graded QW cell structure is taken to be 18%, and is calculated by averaging the QW compositions weighted by the thickness of each QW:

$$18\% = \frac{10\%\times 8nm + 17\%\times 8nm + 23\%\times 6nm + 30\%\times 4nm}{8nm + 8nm + 6nm + 4nm}, \tag{4-1}$$

which is a more conservative estimate compared to simply averaging over the indium concentration of each QW, which would then yield 20% as the average indium concentration.

Figure 4.5(a) shows the measured current density-voltage characteristics for the GaAs *p-i-n* homojunction cell and GaAs/InGaAs QW cells under AM1.5G, 1-sun illumination. Figure 4.5(b) shows the measured external quantum efficiency (E.Q.E.) for the full set of devices, including the GaAs homojunction cell and GaAs/InGaAs QW cells integrated with nanostructured rear contacts. The GaAs/$In_{0.3}Ga_{0.7}As$ QW cell yields the

highest E.Q.E. at wavelengths in the sub-GaAs region where optical absorption primarily occurs in the QW region, but also shows the largest degradation in V_{oc} among this set of devices. The graded QW cell shows slightly lower E.Q.E. in the sub-GaAs bandgap region compared to the GaAs/$In_{0.3}Ga_{0.7}As$ cell, but substantially higher E.Q.E. compared to other reference cells, which maintains E.Q.E. larger than 4% up to 980nm, significantly exceeding the 1% per QW level typically observed. Here we note that because of the strong excitonic absorption near the QW absorption edge, [102] combined with strong coupling of incident light into optical waveguide modes in the thin-film semiconductor layer at ~ 930nm, the measured E.Q.E. in this wavelength range, as well as the measured J_{sc} for the GaAs/$In_{0.1}Ga_{0.9}As$ QW cell, is unusually high compared to those for other QW cells in this study. These observations are consistent with predictions derived from 1D Poisson calculations.

Figure 4.6(a) and (b) show the measured V_{oc} and J_{sc} for the full set of devices versus the QW indium content in each device, respectively. For the graded QW cell, the QW indium concentration is taken to be the average In concentration in the four QWs present in the device. A steady decrease in V_{oc} from 0.92V to 0.52V is observed with increasing the QW concentration in the QW cells for the GaAs homojunction, GaAs/$In_{0.1}Ga_{0.9}As$ QW cell, GaAs/$In_{0.18}Ga_{0.82}As$ QW cell, and the GaAs/$In_{0.3}Ga_{0.7}As$ QW cell. This trend observed in this study is consistent with others reported elsewhere. [103, 104] Similarly, a slight decrease in fill factor is observed for increasing the In concentration in QW solar cells. [34, 90] For the measurements in Figure 4.6(a), the fill factors are 76.9% for the GaAs homojunction reference cell, 71.3% for the GaAs/$In_{0.18}Ga_{0.82}As$ QW cell, and 63.7% for the GaAs/$In_{0.3}Ga_{0.7}As$ QW cell. Compared

to the GaAs/In0$_{.18}$Ga$_{0.82}$As QW cell which has the average In concentration in the QWs, the graded cell has a slightly higher fill factor of 73.8%. In addition, the graded QW cell, with an average 18% In concentration in the QWs, shows both improved V_{oc} (70mV increase) and J_{sc} (0.21mA/cm^2 increase) compared to the GaAs/In$_{0.18}$Ga$_{0.82}$As QW cell. We see that the graded QW cell structure enables V_{oc} and J_{sc}, simultaneously, to surpass the trend lines observed for GaAs/InGaAs QW cells with constant In concentration in the QWs.

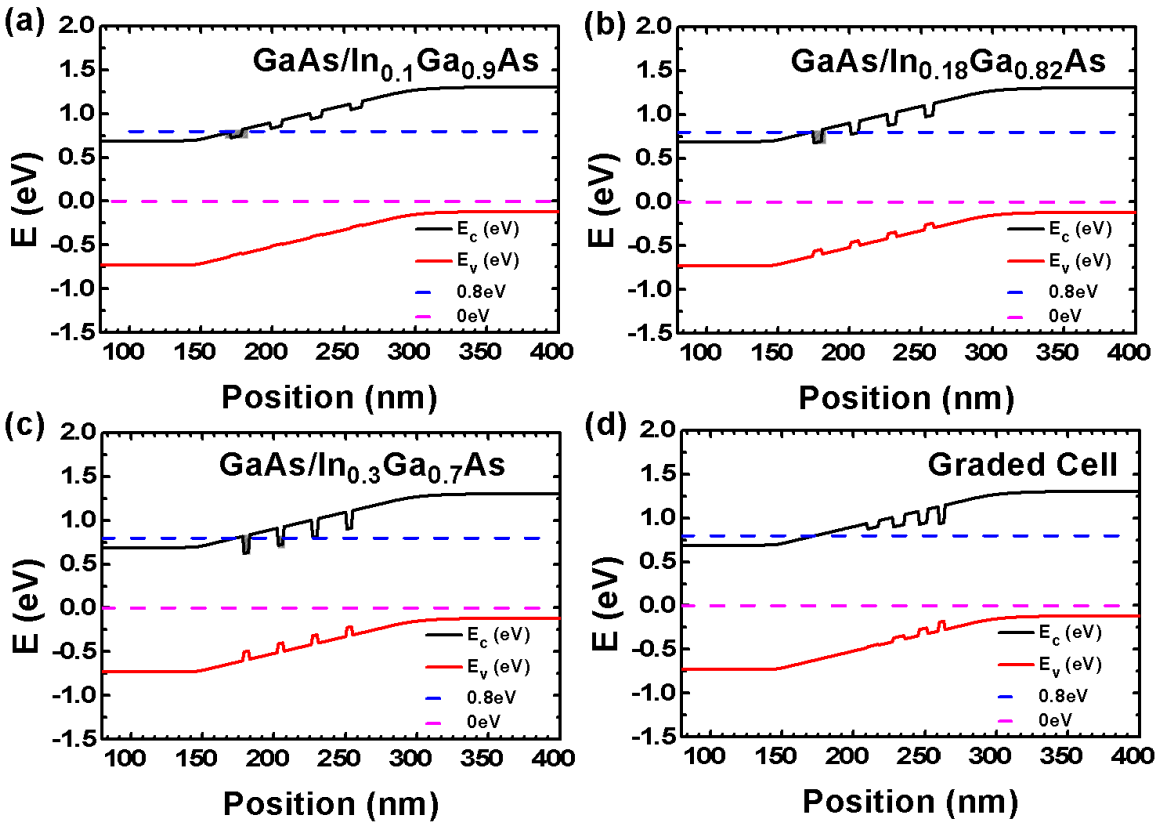

Figure 4.4. 1D Poisson simulation results of band-edge energy diagrams of (a) GaAs/$In_{0.1}Ga_{0.9}As$ QW cell structure; (b) GaAs/$In_{0.18}Ga_{0.82}As$ QW cell structure; (c) GaAs/$In_{0.3}Ga_{0.7}As$ QW cell structure; and (d) graded QW cell structure at a forward bias of 0.8V. Grey areas indicate regions that electron QFL stays above the QW conduction band-edge.

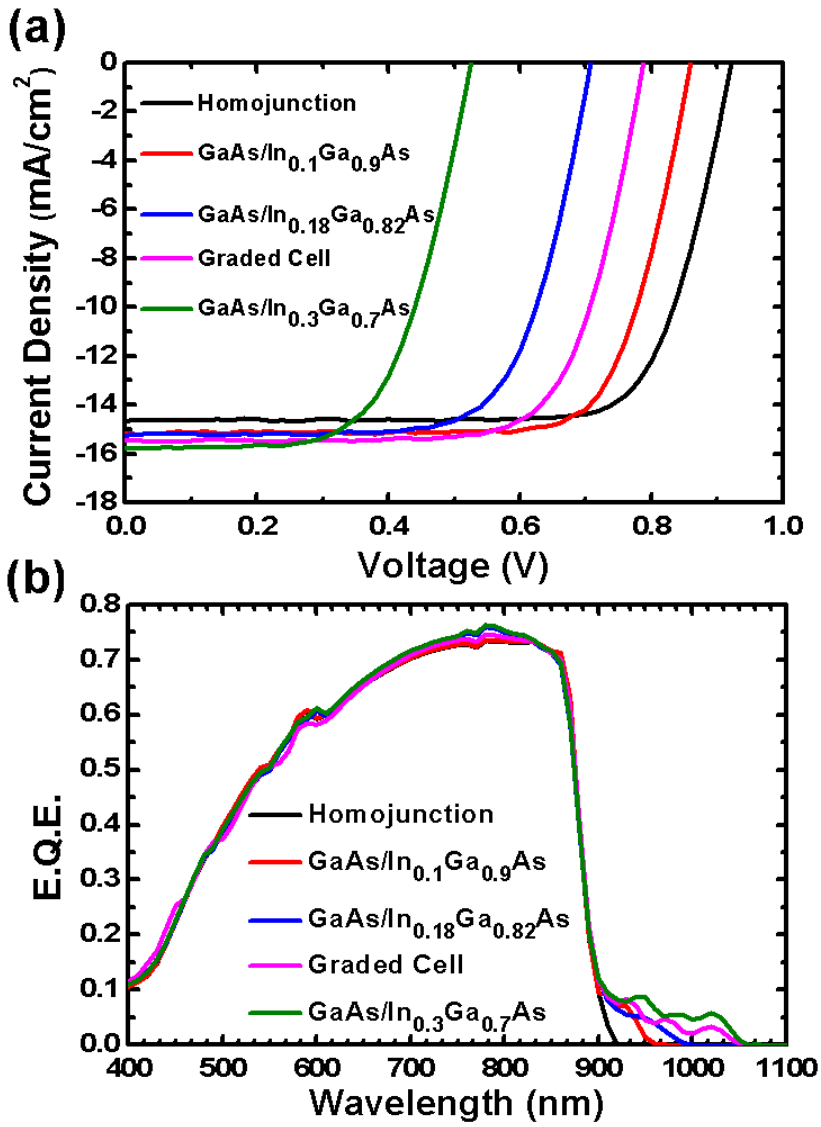

Figure 4.5. (a) Current density-voltage characteristics measured under AM1.5G, 1-sun illumination from a solar simulator for the GaAs *p-i-n* homojunction cell and GaAs/InGaAs QW cells with nanostructured rear contacts. (b) Measured photocurrent response spectra of devices of each type.

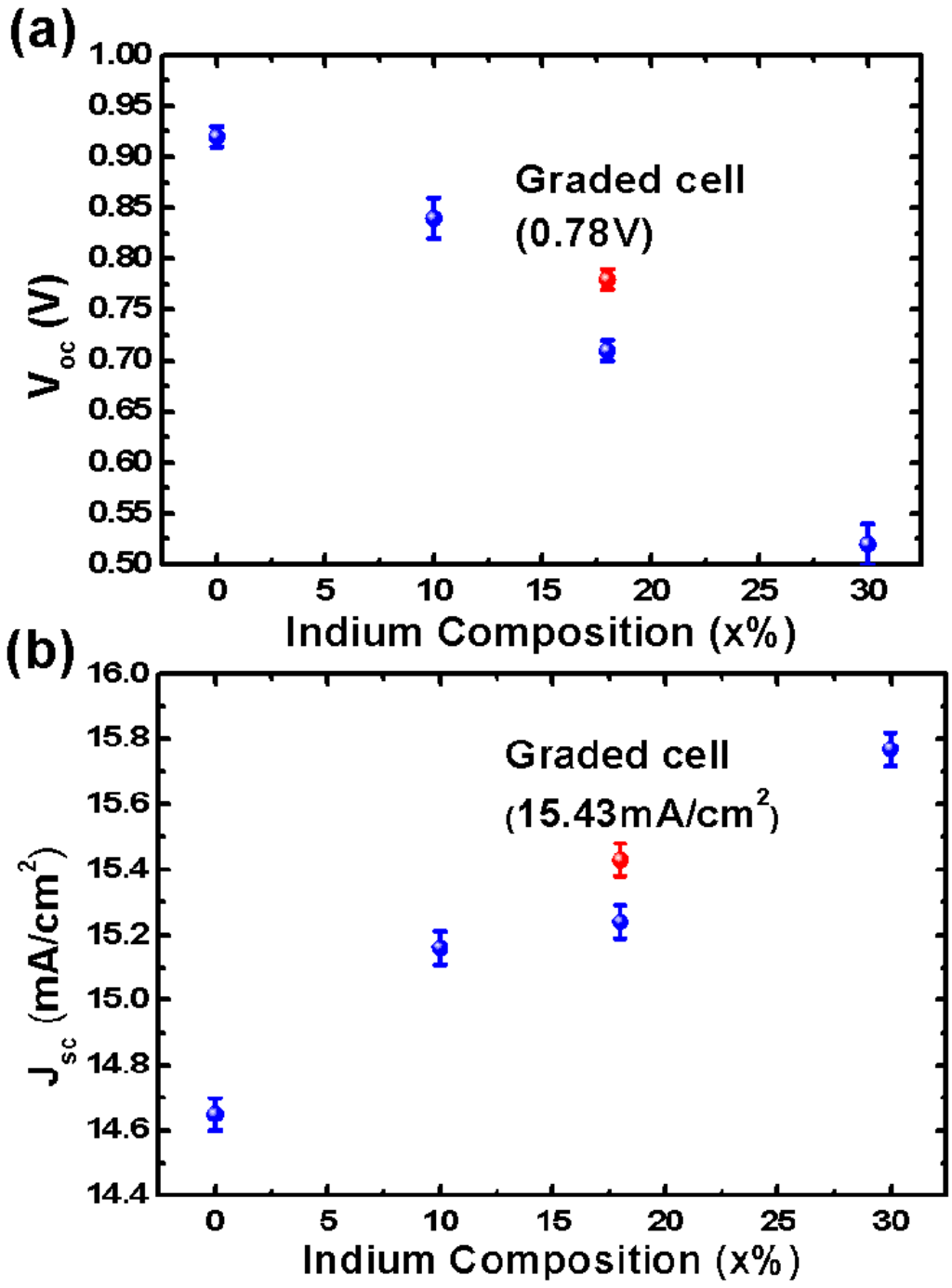

Figure 4.6. (a) and (b) Measured V_{oc} and J_{sc} versus the QW indium content of each cell, respectively.

4.3 Conclusion

We have demonstrated a bandgap engineering strategy for GaAs/InGaAs thin-film QW solar cells with graded QW depths, which is shown to increase both V_{oc} and J_{sc} compared to a QW solar cell with constant QW composition at the same average composition as the QW solar cell with graded QW depths. 1D Poisson calculations show that for the QW solar cell with graded QW depths, the electron QFL stays well above the QW conduction band-edge at a forward bias near its V_{oc} compared to other QW solar cells in this study, which ensures a low concentration of photo-generated carrier density inside QWs at this forward bias. Measurements show that V_{oc} of the GaAs homojunction solar cell and QW solar cells decrease significantly with increasing the indium content in QWs, while the graded QW solar cell, with an average indium concentration of 18% in the QWs, yields both improved V_{oc} and J_{sc} compared to the GaAs/$In_{0.18}Ga_{0.82}As$ QW solar cell. The integration of backside light scattering structures helps further increase the sub-GaAs bandgap wavelength absorption, where absorption primarily occurs in the QW region. It is observed that the for the graded QW solar cell, the absorption extends up to 1050nm, and maintains a greater than 1% E.Q.E. per QW up to 980nm. Thus, this approach shows promise for further improving the performance of QW solar cells, particularly for those with deep QWs, in terms of maintaining both high V_{oc} and J_{sc} values under solar illumination. We anticipate that the V_{oc} of QW solar cells with graded QW depths can be further improved by thinning the QW barriers or employing other strategies to further increase the photo-generated carrier extraction efficiency via increase photo-generated carrier tunneling transport. This approach may be implemented in more complex QW systems, such as ternary or quaternary QW systems, where large

conduction and valence band offsets can be simultaneously achieved by adjusting the QW material composition to further increase the range of absorbed wavelengths while maintaining a minimal reduction in V_{oc}.

Chapter 5: Conclusions and Future Work

This dissertation has covered various areas of research in photovoltaic technologies, including light trapping strategies in thin-film III/V solar cells via light scattering nanostructures created on the front and back side of photovoltaic devices; integrated optical nanostructures for broad-spectrum, omnidirectional antireflection performance in bulk and thin-film III/V solar cells; and novel bandgap engineering strategies for thin-film GaAs/InGaAs quantum well solar cells.

Chapter 2 summarizes a series of works on designing, modeling, and creating metal/dielectric light scattering nanostructures on the front and back side of thin-film GaAs/$In_{0.3}Ga_{0.7}As$ quantum well solar cells. In the study of TiO_2 nanoisland structures created on the surface of thin-film GaAs/$In_{0.3}Ga_{0.7}As$ quantum well solar cells, improvements in both antireflection performance and the quantum well sub-GaAs bandgap photon absorption are achieved thanks to the light scattering properties of the TiO_2 nanoisland structure. From experimental measurements, it is observed that the thin-film GaAs/$In_{0.3}Ga_{0.7}As$ QW solar cell with nanostructured TiO_2 antireflection coating yields ~ 5.8% increase in J_{sc} compared to the same device but with conventional single-layer silicon nitride thin-film antireflection coating. From the analysis of electric field distributions, it is revealed that absorption peaks in the sub-GaAs bandgap region are either associated with Fabry-Perot resonances or optical guided modes. In the study of metal/dielectric light scattering structures on the back side of thin-film GaAs/$In_{0.3}Ga_{0.7}As$ quantum well solar cells, as high as 2.9% per quantum well external quantum efficiency is achieved, significantly surpassing the 1% per quantum well external quantum efficiency typically observed. In addition, light trapping mechanisms of nanostructured

rear contacts have been studied under normal and off-normal conditions both numerically and experimentally, and angular dependences of Fabry-Perot resonance modes and optical guided modes have been clearly revealed. Possible future works could emphasize 1) Optimization and experimental realization of combined front and back side light scattering structures on thin-film III/V quantum well solar cells, and 2) realization of light scattering structures on thin-film solar cells with different materials, such as a-Si:H or nc-Si.

Chapter 3 summarizes a series of works on advanced antireflection strategies on bulk and thin-film flexible, epitaxial lift-off GaAs solar cells via integrated optical nanostructures. In the study of integrated optical nanostructures on bulk single-junction GaAs solar cells, analysis optimization processes for structural feature sizes of double-side moth-eye textured PET packaging sheet and Al_2O_3 nanoisland structure have been demonstrated. From transmittance measurements for moth-eye textured PET packaging sheet of 200nm period with different texturing depths, it is observed that structures with texturing depth of 400nm provide the optimum antireflection performance, maintaining > 90% transmittance at the wavelength range of 400nm to 1050nm at normal incidence, and maintaining > 70% transmittance at the wavelength range of 500nm to 900nm at 80^o incidence. From detailed numerical simulation, it is known that the optimum antireflection performance of Al_2O_3 nanoisland structure is achieved with PS spheres with diameters greater than 500nm, and the antireflection performance differs very little with sphere diameters greater than 500nm. Calculated J_{sc} derived from E.Q.E. measurements shows that the single-junction GaAs solar cell with Al_2O_3 nanoislands integrated with a moth-eye textured PET packaging sheet yields ~ 10% increase in J_{sc}

compared to the reference cell without antireflective optical nanostructures at normal incidence, while ~ 67% increase at 80^o incidence is observed. In the study of integrated optical nanostructures on flexible, epitaxial lift-off GaAs solar cells, GaAs solar cells integrated with Al_2O_3 nanoisland structure and double-side moth-eye textured PET packaging sheet is observed to yield ~ 9% increase in J_{sc} at normal incidence compared to the reference cell without optical nanostructures, and ~ 52% increase in J_{sc} at 80^o angle of incidence. Current-voltage characteristics for the GaAs cell integrated with optical nanostructures and the reference cell without optical nanostructures under both flat and bent conditions have been measured. It is observed that the epitaxial lift-off cell completely integrated with optical nanostructures yields a J_{sc} of ~ 18.14mA/cm^2 at flat condition, and a reduction in J_{sc} of ~ 6.7% at bent condition; while the epitaxial lift-off reference cell without optical nanostructures yields a J_{sc} of ~ 16.20mA/cm^2 at flat condition, and a reduction in J_{sc} of ~ 9.7% at bent condition. In addition, superior self-cleaning properties of moth-eye textured PET packaging sheet have been demonstrated. Possible future work could emphasize implementing this advanced antireflection strategy on a larger scale via approaches such as roll-to-roll nanoimprint lithography technique.

Chapter 4 summarizes the study of novel bandgap engineering strategies on GaAs/InGaAs quantum well solar cells with graded quantum well depths. 1D Poisson calculations show that for the QW solar cell with graded QW depths, the electron QFL stays well above the QW conduction band-edge at a large forward bias near its V_{oc} compared to other reference QW solar cells, which ensures a low concentration of photo-generated carrier density inside QWs at this forward bias. Experimental measurements show that the quantum well solar cell with graded quantum well depths yields both

improved J_{sc} (0.21mA/cm^2) and V_{oc} (70mV) compared to the GaAs/$In_{0.18}Ga_{0.82}As$ quantum well solar cell which has the same average indium concentration in the quantum well region as the graded quantum well solar cell. Possible future works could emphasize 1) Further optimization of the graded quantum well structure, such as facilitating the tunneling transport of photo-generated carriers by thinning the quantum well barriers via strain-balance techniques, and 2) applying this idea to more complex quantum well systems where large conduction and valence band offsets can be simultaneously achieved by adjusting the quantum well material composition.

References

1. N. J. Ekin-Daukes, K. W. J. Barnham, J. P. Connolly, J. S. Roberts, J. C. Clark, G. Hill, and M. Mazzer, *Appl. Phys. Lett.* **75**, 4195 (1999).
2. A. Luque, A. Marti, and C. Stanley, *Nat. Photon.* **6**, 146 (2012).
3. K. A. Sablon, J. W. Little, V. Mitin, A. Sergeev, N. Vagidov, and K. Reinhardt, *Nano Lett.* **11**, 2311 (2011).
4. H. Cotal, C. Fetzer, J. Boisvert, G. Kinsey, R. King, P. Hebert, H. Yoon, and N. Karam, *Energy Environ. Sci.* **2**, 174 (2009).
5. M. Yamaguchi, *Sol. Energy Mater. Sol. Cells* **75**, 261 (2003).
6. M. Konagai, M. Sugimoto, and K. Takahashi, *J. Cryst. Growth*, **45**, 277 (1978).
7. G. J. Bauhuis, P. Mulder, E. J. Havercamp, J. C. C. M. Huijben, and J. J. Schermer, *Sol. Energy. Mater. Sol. Cells* **93**, 1488 (2009).
8. J. Yoon, S. Jo, I. S. Chun, I. Jung, H. –S. Kim, M. Meitl, E. Menard, X. Li, J. J. Coleman, U. Paik, and J. A. Jogers, *Nature (London)* **465**, 329 (2010).
9. R. Winston, J. C. Minano, and P. Benitez, *Nonimaging Optics*, Elsevier Academic Press (2005).
10. K. M. Trautz, P. P. Jenkins, R. J. Walters, D. Scheiman, R. Hoheisel, R. Tatavarti, R. Chan, H. Miyamoto, J. G. J. Adams, V. C. Elarde, and J. Grimsley, *IEEE J. Photovoltaics* **3**(1), 535 (2013).
11. H. Atwater and A. Polman, *Nat. Mater.* **9**. 205 (2010).
12. Z. Yu, A. Raman, and S. Fan, *Proc. Natl. Acad. Sci. U. S. Am.* **107**, 17491 (2010).
13. D. M. Schaadt, B. Feng, and E. T. Yu, *Appl. Phys. Lett.* **86**, 063106 (2005).
14. D. Derkacs, S. H. Lim, P. Matheu, W. Mar and E. T. Yu, *Appl. Phys. Lett.* **89**, 093103 (2006).
15. M. Berginski, J. Hupkes, M. Shulte, G. Schope, H. Stiebig, B. Rech, and M. Wuttig, *J. Appl. Phys.* **101**, 074903 (2007).
16. J. Zhu, C. –M. Hsu, S. Fan, and Y. Cui, *Nano Lett.* **10**, 1979 (2010).
17. X. H. Li, P. –C. Li, D. Z. Hu, D. Schaadt, and E. T. Yu, *J. Appl. Phys.* **115**, 044303 (2014).
18. D. Derkacs, W. V. Chen, P. M. Matheu, S. H. Lim, P. K. L. Yu, and E. T. Yu, *Appl. Phys. Lett.* **93**, 091107 (2008).
19. C. Rockstuhl, F. Lederer, K. Bittkau, and R. Carius, *Appl. Phys. Lett.* **91**, 171104 (2007).
20. E. Klampaftis, D. Ross, K. R. McIntosh, and B. S. Richards, *Sol. Energy Mater. Sol. Cells* **93**, 1192 (2009).
21. H. Hoppe, N. Arnold, N. S. Sariciftci, and D. Meissner, *Sol. Energy Mater. Sol. Cells* **80**, 105 (2003).
22. H. A. McLeod, *Thin-Film Optical Filters*, CRC Press, New York (2010).
23. X. Yan, D. J. Poxson, J. Cho, R. E. Welser, A. K. Sood, J. K. Kim, and E. F. Schubert, *Adv. Funct. Mater.* **23**, 583 (2013).
24. H. Park, D. Shin, G. Kang, S. Baek, K. Kim, and W. J. Padilla, *Adv. Mater.* **23**, 5796 (2011).
25. J. Y. Chen, M. H. Yu, S. F. Chang, and K. W. Sun, *Appl. Phys. Lett.* **103**, 133901 (2013).

26. P. –C. Li and E. T. Yu, *J. Opt. Sci. Am. B.* **30**, 2584 (2013).
27. K. Choi, S. H. Park, Y. M. Song, Y. T. Lee, C. K. Hwangbo, H. Yang, and H. S. Lee, *Adv. Mater*. **22**, 3713 (2010).
28. K. Barnham, I. Ballard, J. Barnes, J. Connolly, P. Griffin, B. Kluftinger, J. Nelson, E. Tsui, and A. Zachariou, *Appl. Surf. Sci*. **113/114**, 722 (1997).
29. D. Derkacs, W. V. Chen, P. M. Matheu, S. H. Lim, P. K. L. Yu and E. T. Yu, *App. Phys. Lett*. **93**, 091117 (2008).
30. D. B. Bushnell, N. J. Ekins-Daukes, K. W. J. Barnham, J. P. Connolly, J. S. Roberts, G. Hill, R. Airey, and M. Mazzer, *Sol. Energ. Mater. Sol. Cell.* **75**, 299 (2003).
31. K. Tanabe, K. Watanabe, and Y. Arakawa, *Appl. Phys. Lett*. **100**, 192102 (2012).
32. M. F. Bennett, Z. S. Bittner, D. V. Forbes, S. R. Tatavarti, S. P. Ahrenkiel, A. Wibowo, N. Pan, K.Chern and S. M. Hubbard, *Appl. Phys. Lett*. **103**, 213902 (2013).
33. R. Dahal, J. Li, K. Aryal, J. Y. Lin and H. X. Jiang, *Appl. Phys. Lett*. **97**, 073115 (2010).
34. K. Y. Lai, G. J. Lin, Y. –L. Lai, Y. F. Chen and J. H. He, *Appl. Phys. Lett*. **96**, 081103 (2010).
35. K. W. J. Barnham, B. Braun, J. Nelson, M. Paxman, C. Button, J. S. Roberts and C. T. Foxon, *Appl. Phys. Lett*. **59**, 135 (1991).
36. N. G. Anderson, *J. Appl. Phys*. **78**, 1850 (1995).
37. R. Corkish and M. A. Green, *IEEE Photovolt. Spec. Conf., 23th*, 675 (1993).
38. P. –H. Wu, Y. –K. Su, I. –L. Chen, C. –H. Chiou, J. –T. Hsu and W. –R. Chen, *Jpn. J. Appl. Phys*. **45**, 25 (2006).
39. Y. Wang, S. Ma. K. Watanabe, M. Sugiyama and Y. Nakano, *J. Cryst. Growth* **352**, 194-198 (2012).
40. Y. Wen, Y. Wang, K. Watanabe, M. Sugiyama and Y. Nakano, *IEEE. J. Photovolt*. **2**, 2 (2012).
41. A. Shah, P. Torres, R. Tscharner, N. Wyrsch, and H. Keppner, *Science* **285**, 692 (1999).
42. K. L. Chopra, P. D. Paulson and V. Dutta, *Prog. Photovoltaics* **12**, 69 (2004).
43. H. Jason, Meint de Boer, J. Burger, R. Legtenberg and M. Elwenspoek, *Microelectron. Eng.* **27**, 475 (1995).
44. V. E. Ferry, M. A. Verschuuren, H. B. T. Li, R. J. Walters, R. E. I. Schropp, H. A. Atwater and A. Polman, *Opt. Express* **18**, A237 (2010).
45. E. T. Yu and J. van de Lagemaat, *MRS Bulletin* **36**, 424 (2011).
46. K. Tanabe, K. Watanabe, and Y. Arakawa, *Appl. Phys. Lett.* **100**, 192102 (2012).
47. J. Rybczynski, U. Ebels, and M. Giersig, *Colloids Surf.* **219**, 1 (2003).
48. S. Chhajed, M. F. Schubert, J. K. Kim, and E. F. Schubert, *Appl. Phys. Lett.* **93**, 251108 (2008).
49. W. H. Southwell, *J. Opt. Soc. Am.* **8**, 549 (1991).
50. C. H. Sun, W. L. Min, C. H. Lin, P. Jiang, and B. Jiang, *Appl. Phys. Lett.* **91**, 231105 (2007).
51. S. M. Sze, *Physics of Semiconductor Devices* (John Wiley & Sons, New York, 1981), pp. 800 – 805.
52. P. Spinelli, V. E. Ferry, J. van de Groep, M. van Lare, M. A. Verschuuren, R. E. I. Schropp, H. A. Atwater, and M. Mazzer, *J. Opt.* **14**, 024002 (2012).

53. X. H. Li, P. –C. Li, D. Hu, D. M. Schaadt, and E. T. Yu, *Appl. Phys. Lett.* **114**, 044310 (2013).
54. H. A. Macleod, *Thin-Film Optical Filters*, CRC Press, New York, 2010.
55. A. Luque and A. Marti, *Prog. Photovoltaics* **9**, 73 (2001).
56. D. C. Johnson, I. M. Ballard, K. W. J. Barnham, J. P. Connolly, M. Mazzer, A. Bessiere, C. Calder, G. Hill, and J. S. Roberts, *Appl. Phys. Lett.* **90**, 213505 (2007).
57. R. R. King, D. C. Law, K. M. Edmondson, C. M. Fetzer, G. S. Kinsey, H. Yoon, R. A. Sherif, and N. H. Karam, *Appl. Phys. Lett.* **90**, 183516 (2007).
58. J. F. Geisz, D. J. Friedman, J. S. Ward, A. Duda, W. J. Olavarria, T. E. Moriarty, J. T. Kiehl, M. J. Romero, A. G. Norman, and K. M. Jones, *Appl. Phys. Lett.* **93**, 123505 (2005).
59. H. Cotal, C. Fetzer, J. Boisvert, G. Kinsey, R. King, P. Hebert, H. Yoon, and N. Karam, *Energy Environ. Sci.* **2**, 174 (2009).
60. M. Yamaguchi, *Sol. Energy Mater. Sol. Cells* **75**, 261 (2003).
61. K. L. Chopra, P. D. Paulson, and V. Dutta, *Prog. Photovoltaics* **12**, 69 (2004).
62. R. Tatavarti, A. Wibowo, G. Martin, F. Tuminello, C. Youtsey, G. Hiller, N. Pan, M. W. Wanlass, and M. Romero, *35th IEEE Photovoltaic Specialists Conference (PVSC) conference* 002125-002128 (2010).
63. J. J. Schermer, G. J. Bauhuis, P. Mulder, W. J. Meulemeesters, E. Haverkamp, M. M. A. J. Voncken, and P. K. Larsen, *Appl. Phys. Lett.* **76**, 2131 (2000).
64. E. Yablonovitch, T. J. Gmitter, J. P. Harbison, and R. Bhat, *Appl. Phys. Lett.* **51**, 2222 (1987).
65. J. Yoon, S. Jo, I. S. Chun, I. Jung, H. –S. Kim, M. Meitl, E. Menard, X. Li, J. J. Coleman, U. Paik, and J. A. Rogers, *Nature* **465**, 329 (2010).
66. R. Tatavarti, G. Hillier, A. Dzankovic, G. Martin, F. Tuminello, R. Navaratnarajah, G. Du, D. P. Vu, and N. Pan, *33rd IEEE Photovoltaic Specialists Conference (PVSC) conference* 1-4 (2008).
67. J. J. Schermer, P. Mulder, G. J. Bauhuis, P. K. Larsen, G. Oomen, and E. Bongers, *Prog. Photovoltaics* **13**, 587-596 (2005).
68. K. T. Shiu, J. Zimmerman, H. Y. Wang, and S. R. Forrest, *Appl. Phys. Lett.* **95**, 223503 (2009).
69. N. Pan, *IEEE International Conference on Semiconductor Electronics (ICSE)* 347-349 (2014).
70. E. D. Palik, *Handbook of Optical Constants of Solids* (Academic Press, New York, 1998).
71. X. H. Li, P. –C. Li, L. Ji, C. Stender, C. McPheeters, S. R. Tatavarti, K. Sablon, and E. T. Yu, Prog. Photovoltaics DOI: 10.1002/pip2565 (2014).
72. Y. Liu, A. Das, S. Xu, Z. Lin, C. Xu, Z. L. Wang, A. Rohatgi, and C. P. Wong, *Adv. Energy Mater.* **2**, 47-51 (2012).
73. Y. B. Park, H. Im, M. Im, Y. K. Choi, *J. Mater. Chem.* **21**, 633-636 (2011).
74. L. K. Verma, M. Sakhuja, J. Son, A. J. Danner, H. Yang, H. C. Zeng, and C. S. Bhatia, *Renewable Energy* **36**, 2489-2493 (2011).
75. W. L. Min, B. Jiang, and P. Jiang, *Adv. Mater.* **20**, 3914-3918 (2008).
76. S. A. Boden, and D. M. Bagnall, *Appl. Physic. Lett.* **93**, 133108 (2008).
77. C. Chen, G. Hubbarb, P. A. Shields, C. Liu, D. W. E. Allsopp, W. N. Wang, and S. Abbott, *Appl. Phys. Lett.* **94**, 263118 (2009).

78. J. H. Shin, K. S. Han, and H. Lee, *Prog. Photovoltaics* **19**, 339-344 (2011).
79. S. Nishimoto, and B. Bhushan, *RSC Advances* **6**, 671-690 (2013).
80. Y. R. Lin, H. P. Wang, C. A. Lin, J. H. He, *J. Appl. Phys.* **106**, 114310 (2009).
81. S. H. Ahn, and L. J. Guo, *Adv. Mater.* **20**, 2044-2049 (2008).
82. M. G. Kang, M. S. Kim, J. Kim, and L. J. Guo, *Adv. Mater.* **20**, 4408-4413 (2008).
83. X. Zhang, A. Hosseini, A. Lin, H. Subbaraman, and R. T. Chen, *IEEE J. Sel. Topics Quantum Electron.* **19**, 196-210 (2013).
84. S. Ahn, J. Cha, H. Myung, S. M. Kim, and S. Kang, *Appl. Phys. Lett.* **89**, 213101 (2006).
85. R. C. Knechtli, R. Y. Loo, and G. S. Kamath, *IEEE Trans. Electron Devices* **31**, 577 (1984).
86. W. Shockley and H. Queisser, *J. Appl. Phys.* **32**, 510 (1961).
87. C. H. Henry, *J. Appl. Phys.* **51**, 4494 (1980).
88. M. A. Green, K. Emery, Y. Hishikawa, W. Warta, and D. Dunlop, *Prog. Photovoltaics* **22**, 1-9 (2014).
89. J. C. Zolper and A. M. Barnett, *IEEE Trans. Electron Devices* **37**, 478-484 (1990).
90. R. Dahal, B. Pantha, J. Li, J. Y. Lin, and H. Jiang, *Appl. Phys. Lett.* **94**, 063505 (2009).
91. S. M. Ramey and R. Khoie, *IEEE Trans. Electron Devices* **50**, 5 (2003).
92. M. Mazzer, K. W. J. Barnham, I. M. Ballard, A. Bessiere, A. Ioannides, D. C. Johnson, M. C. Lynch, T. N. D. Tibbits, J. S. Roberts, G. Hill, and C. Calder, *Thin Solid Films* **76**, 511-512 (2006).
93. A. Alemu, J. A. H. Coaquira, and A. Freundlich, *J. Appl. Phys.* **99**, 084506 (2006).
94. J. G. J. Adams, B. C. Browne, I. M. Ballard, J. P. Connolly, N. L. A. Chan, A. Ioannides, W. Elder, P. N. Stavrinou, K. W. J. Barnham, and N. J. Ekins-Daukes, *Prog. Photovoltaics* **19**, 865-877 (2011).
95. R. Oshima, A. Takata, and Y. Okada, *J. Appl. Phys.* **93**, 083111 (2008).
96. N. J. Ekins-Daukes, K. –H. Lee, L. Hirst, A. Chan, M. Führer, J. Adams, B. Browne, K. W. J. Barnham, P. Stavrinou, J. Connolly, J. S. Roberts, B. Stevens, R. Airey, and K. Kennedy, *J. Phys. D: Appl. Phys.* **46**, 264007 (2013).
97. G. Snider, 1D Poisson Program (PC version beta 8), University of Notre Dame, see http://www.nd.edu/~demand.
98. X. H. Li, V. D. Dasika, P. –C. Li, L. Ji, S. R. Bank, and E. T. Yu, *Appl. Phys. Lett.* **105**, 123906 (2014).
99. M. Courel, J. Rimada, and L. Hernandez, *Prog. Photovoltaics* **21**, 276 (2013).
100. U. Rau, *Phys. Rev. B* **76**, 085303 (2007).
101. N. J. Ekins-Daukes, C. D. J. Calder, I. Ballard, K. W. J. Barnham, J. Nelson, J. S. Roberts, and G. Hill, in *Proceedings of 3rd World Conference on Photovoltaic Energy Conversion (2003)*, p. 2702.
102. C. O. McPheeters, D. Hu, D. M. Schaadt, and E. T. Yu, *J. Opt.* **14**, 024007 (2012).
103. X. Zhang, X. Wang, H. Xiao, C. Yang, Q. Hou, H. Yin, H. Chen, and Z. Wang, *Chin. Phys. B* **20**, 028402 (2011).
104. I. Serdiukova, C. Monier, M. F. Vilela, and A. Freundlich, *Appl. Phys. Lett.* **74**, 2812 (1999).